https://doi.org/10.5194/egusphere-2026-2299
Preprint. Discussion started: 24 June 2026

CIR Process Age Inference Algorithm v1.0: scalable and consistent sedimentation rate modeling for ocean sediment cores via the Cox-Ingersoll-Ross process

Taehee Lee[1], Lorraine E. Lisiecki[2], Samuel R. Newall[2], Yuxin Zhou[3], and Charles E. Lawrence[4]

[1]Department of Earth, Environmental & Planetary Sciences, Brown University
[2]Department of Earth Science, University of California, Santa Barbara
[3]School of Earth and Atmospheric Sciences, Georgia Institute of Technology
[4]Division of Applied Mathematics, Brown University

Correspondence: Taehee Lee (taehee_lee@brown.edu)

Abstract. Deep-sea sediment cores provide a key archive of past climate, with geochemical measurements of microfossils providing both environmental information and age constraints; however, constructing continuous age-depth models is challenging due to sparse and uncertain direct dating (e.g., radiocarbon up to 50 kyr BP) and the need to integrate more densely sampled but indirect proxies such as benthic $\delta^{18}O$, which requires pattern alignment to reference stacks while maintaining physically plausible sediment rates. Bayesian frameworks have therefore become standard, with approaches such as BACON (Blaauw and Christen, 2011) that models inverse sedimentation rates via an autoregressive gamma process and BIGMACS (Lee et al., 2023) that integrates both direct and indirect constraints through probabilistic alignment and empirically informed priors. Despite their practical utilities, these method exhibit key limitations: BACON relies heavily on user-specified hyperparameters that are not statistically inferred from the data, while BIGMACS could employ a sedimentation-rate model defined on uneven depth grids, potentially leading to inconsistent smoothness and sensitivity to proxy resolution. Here we propose the Cox-Ingersoll-Ross (CIR) Process Age Inference Algorithm to tackle the aforementioned limitations. This multi-layer Bayesian hierarchical framework employs the CIR process as a prior on the inverse sedimentation rates to guarantee a consistent smoothness over depths to address the drawback of BIGMACS, and it allows estimation of the CIR process model parameters via the Expectation-maximization (EM) algorithm. To validate our framework, we first estimated the model parameters from a carefully curated dataset of 79 radiocarbon records, and then applied the algorithm to four other radiocarbon-dated benthic $\delta^{18}O$ sediment core records to compare the performance to BIGMACS. The resulting age models not only show greater consistency and robustness but also preserve smoothness of posterior sedimentation rates over depths and successfully avoid alignment artifacts.

1 Introduction

Ocean sediments collected by deep sea coring provide an important archive of past climate data. Geochemical measurements of microfossils within the sediment provide information about the local and global climate state at the time when the microfossil formed and, in some cases, an estimate of how many years ago that was. Developing age estimates continuously as a function

https://doi.org/10.5194/egusphere-2026-2299
Preprint. Discussion started: 24 June 2026

of depth is an important process that allows paleoclimate scientists to evaluate when climate and oceanographic changes are observed in different parts of the ocean as well as the rate at which these changes occur (Westerhold et al., 2024).

The construction of accurate age models presents considerable challenges, primarily due to the sparse sampling of direct age indicators and their associated uncertainties. In this study, we focus predominantly on radiocarbon dating, which provides reliable age constraints for deposits up to approximately 50 kiloyears before present (kyr BP) (Heaton et al., 2020). An alternative strategy leverages more densely sampled proxy records that respond to global climate variability and therefore exhibit broadly synchronous behavior across cores – such as the oxygen isotope composition of benthic foraminiferal carbonate, commonly denoted as benthic $\delta^{18}O$ (e.g., Lisiecki and Raymo (2005)). We refer to such indicators as *indirect* proxies, in contrast to those yielding *direct* age estimates.

Whereas direct proxies permit age estimation at individual depths, indirect proxies typically rely on identifying patterns across sequences of observations and matching them to a reference profile that captures shared structures among multiple records. Aligning such patterns to a reference profile requires consideration not only of how well the observations aligned to prominent features of the profile but also of whether the implied sedimentation rates from the resulting age-depth model remain physically plausible (Lin et al., 2014). Balancing these two requirements – accurate pattern alignment and realistic sedimentation dynamics – renders age estimation based on indirect proxies a particularly challenging problem.

To address the above challenges, Bayesian age inference has become a standard framework for reconstructing chronologies of sediment cores in paleoclimatology (Haslett and Parnell, 2008; Blaauw and Christen, 2011). Among widely used approaches, the BACON employs an autoregressive (AR) gamma process to represent sedimentation rates, dividing the core into sections and modeling their rates with a stochastic process that incorporates prior knowledge about sedimentation dynamics. This framework enforces monotonic age-depth relationships and enables realistic interpolation between dated depths while accounting for uncertainty in radiocarbon measurements through Bayesian inference and MCMC sampling (Blaauw and Christen, 2011).

More recently, BIGMACS extends Bayesian age modeling by integrating both direct and indirect sources of chronological information. In addition to radiocarbon ages, it incorporates probabilistic stratigraphic alignment of benthic $\delta^{18}O$ records to a target stack and constrains sedimentation rate variability using empirically derived priors from marine sediment cores. By combining absolute age constraints from radiocarbon dating with relative chronological information from proxy alignment within a unified Bayesian framework, BIGMACS enables the construction of multiproxy age models and regional proxy stacks with improved chronological precision and quantified uncertainty (Lee et al., 2023).

However, both BACON and BIGMACS have their own limitations. In BACON, the AR gamma process governing sediment accumulation is strongly influenced by the choice of its hyperparameters. These parameters are not derived or statistically estimated from the data; rather, they are treated primarily as user-specific prior quantities informed by domain knowledge, although the software provides recommended default values. Consequently, the resulting age-depth models can depend substantially on these prior specifications. In BIGMACS, the sedimentation-rate model is formulated as a first-order AR process defined only at the middle points of depths where proxy observations are available, which are generally unevenly spaced. As a result, the inferred sedimentation rates may exhibit inconsistent smoothness across depths, with their behavior becoming sensitive to the local resolution of the proxy observations in each sediment record.

https://doi.org/10.5194/egusphere-2026-2299
Preprint. Discussion started: 24 June 2026

Here we propose a novel age inference algorithm based on a multi-layer Bayesian hierarchical framework, designed to address the limitations of existing methods such as BACON and BIGMACS. The model comprises three principal layers: a prior layer on inverse sedimentation rates, a transformation layer that maps these rates into age-depth models, and a likelihood layer that links proxy observations – direct or indirect – to the inferred ages via a calibration model or a reference stack. By adopting the Cox-Ingersoll-Ross (CIR) process (Cox et al., 1985; Wolpert, 2021) as a prior, our approach not only regularizes sedimentation rates – thereby discouraging implausible extremes or abrupt fluctuations – but also ensures a consistent degree of smoothness over depths that BIGMACS fails to guarantee. The model parameters of the CIR process are estimated from a carefully curated training set of 79 radiocarbon (^{14}C) records after being standardized, enabling the derivation of globally applicable model specifications. Query sedimentation records may then be standardized and integrated into the framework for age estimation. We further validate our method through four real-world case studies, demonstrating its practical efficacy and robustness.

The remainder of this paper is structured as follows. Section 2 introduces the essential background material necessary for a thorough understanding of the modeling framework. Section 3 presents the formulation of our model, details the associated inference procedures, and sets out the proposed algorithms. Section 4 describes the training dataset – comprising 79 sediment records – used to estimate the sedimentation rate model. Section 5 illustrates the age inference results through four representative case studies. Finally, discussion and concluding remarks are provided in Sections 6 and 7, respectively.

2 Background Knowledge

Our Cox-Ingersoll-Ross (CIR) Process Age Inference Algorithm is a statistical inference algorithm that leverages advanced probabilistic techniques. A foundational understanding of the CIR process, which is one of the stationary gamma processes, the Hamiltonian Monte Carlo algorithm, and the Stein variational gradient descent algorithm is essential for understanding its underlying methodology. To facilitate this, we provide a concise introduction to these concepts before presenting our formal model in Section 3. Throughout the manuscript, we adhere to the following notational conventions.

- For a function $f : \mathcal{X} \to \mathbb{R}$ and a *finite* subset $X \subset \mathcal{X}$, f_X is a vector whose entry is $f(x)$ for each $x \in X$.
- For a function $f : \mathcal{X} \times \mathcal{X} \to \mathbb{R}$ and *finite* subsets $X, X' \subset \mathcal{X}$, $f_{XX'}$ is a matrix whose entry is $f(x, x')$ for each $x \in X$ and $x' \in X'$.

2.1 Cox-Ingersoll-Ross Process

A stationary gamma process is a stochastic process (say, X_t, with three parameters, shape α, rate β, and $\rho \in (0, 1)$) that satisfies the following two conditions: (1) the marginal distribution of X_t at each time t is the gamma distribution $Gamma(\alpha, \beta)$; and (2) the correlation function of X_t and X_s is $\rho^{|t-s|}$ for each pair of time t and s, i.e., it only depends on the time increment. Note that the stationary gamma process is not uniquely defined given those parameters: there are at least six different processes (Wolpert, 2021).

One of those stationary gamma processes is the Gamma AR(1) process, which is a discrete approximation of the continuous time Ornstein-Uhlenbeck process with gamma innovation (OU-Γ process) (Barndorff-Nielsen and Shephard, 2003). For instance,

https://doi.org/10.5194/egusphere-2026-2299
Preprint. Discussion started: 24 June 2026

Blaauw and Christen (2011) model the inverse sedimentation rate (i.e., age-over-depth) X_t by $X_t = wX_{t+1} + (1-w)\,\alpha_t$, where $w \in [0,1]$ and $\alpha_t \sim_{i.i.d.} Gamma(\alpha, \beta)$, in their age inference algorithm, BACON. Exact sampling from the OU-Γ process is not straightforward, but still feasible: see (Qu et al., 2021) for more details.

Here, we consider another stationary gamma process, the Cox-Ingersoll-Ross (CIR) process (Cox et al., 1985), to model inverse sedimentation rates. One main distinctive characteristic is that CIR processes are continuous over time, unlike OU-Γ processes which occasionally allow discontinuous jumps. To be more precise, we only consider the gamma process that is specified by the following stochastic differential equation[1] (SDE):

$$dX_t = -\log\rho \cdot \left(\frac{\alpha}{\beta} - X_t\right) \cdot dt + \sqrt{-\frac{2}{\beta}\log\rho} \cdot \sqrt{X_t} \cdot dW_t. \tag{1}$$

Cox et al. (1985) show that the solution of the above SDE satisfies the Markov property and the conditional distribution of X_t given X_s is expressed as the following *closed* form:

$$p(X_t|X_s) = \frac{\beta}{1-\rho^{|t-s|}} \cdot \exp\left(-\frac{\beta}{1-\rho^{|t-s|}}\left(\rho^{|t-s|}X_s + X_t\right)\right) \cdot \left(\frac{X_t}{\rho^{|t-s|}X_s}\right)^{\frac{\alpha-1}{2}} \cdot I_{\alpha-1}\left(\frac{2\beta}{1-\rho^{|t-s|}}\sqrt{\rho^{|t-s|}X_sX_t}\right), \tag{2}$$

where $I_{\alpha-1}$ is the modified Bessel function of the first kind of order $\alpha - 1$.

2.2 Gaussian Process

A Gaussian process (GP) is a stochastic process such that every finite collection of its random variables follows a multivariate normal distribution (Rasmussen and Williams, 2006; Banerjee et al., 2014; Murphy, 2022, 2023). As a tool of Bayesian statistics, it defines a prior on the random latent *function* that relates the input features and output observations. Each GP is completely specified by the mean and kernel covariance function, and, in notation, $f \sim \mathcal{GP}(\mu, \mathbb{K})$ implies that a random function $f : \mathcal{X} \to \mathbb{R}$ follows a GP specified by the mean function $\mu : \mathcal{X} \to \mathbb{R}$ and kernel covariance function $\mathbb{K} : \mathcal{X} \times \mathcal{X} \to \mathbb{R}$ defined in a domain $\mathcal{X}$.

If the kernel function is given as $\mathbb{K}(t,s) \triangleq \exp\left(-\frac{1}{2}\gamma^2 \cdot |t-s|\right)$ for a kernel parameter $\gamma \in \mathbb{R}$ and any $t, s \in \mathbb{R}$, then the associated GP, $\mathcal{GP}(0, \mathbb{K})$, is called the Ornstein-Uhlenbeck Gaussian process (OU-GP). Here, we have an interesting relationship between the OU-GP and the CIR process: for the same α, β and ρ in Section 2.1 where $2\alpha \in \mathbb{N}$, the process,

$$X_t \triangleq \frac{1}{2\beta}\sum_{n=1}^{2\alpha}\left(Z_t^{(n)}\right)^2, \tag{3}$$

where $\left\{Z^{(n)}\right\}_{n=1}^{2\alpha}$ is a set of independent random functions drawn from the above OU-GP for $\gamma \triangleq \sqrt{-\log\rho}$, satisfies the two conditions for being a stationary gamma process and is indeed a CIR process specified by the SDE in Equation (1) (Jeanblanc et al., 2009; Mishura et al., 2024). That is, provided that $2\alpha \in \mathbb{N}$, to sample a CIR process specified by α, β and ρ, one can just draw 2α independent samples from the OU-GP where its kernel parameter is $\sqrt{-\log\rho}$, add up their squares, and divide the sum by 2β.

[1] Note that $\log\rho < 0$ because $\rho \in (0,1)$. Here, W_t is the Wiener process.

https://doi.org/10.5194/egusphere-2026-2299
Preprint. Discussion started: 24 June 2026

2.3 Numerical Integration with the Midpoint Rule

Suppose that a finite set of the realizations of the first-order derivative $\dot{F} = \left\{ \dot{f}\left(\frac{t_n + t_{n+1}}{2}\right) \right\}_{n=1}^{N}$ of a function $f : \mathbb{R} \to \mathbb{R}$ at the middle points of the *strictly increasing* entries $\{t_n \in \mathbb{R}\}_{n=0}^{N}$ of the domain $\mathbb{R}$ under the constraint $f(t_0) = b \in \mathbb{R}$ is given. The simplest approximation of $f(t)$ at $t \in [t_{m-1}, t_m)$ would be:

$$f(t) \approx b + \sum_{n=1}^{m-1} (t_n - t_{n-1}) \cdot \dot{f}\left(\frac{t_{n-1} + t_n}{2}\right) + (t - t_{m-1}) \cdot \dot{f}\left(\frac{t_{m-1} + t_m}{2}\right), \tag{4}$$

which is called the numerical integration with the midpoint rule (Süli and Mayers, 2003). In words, the method assumes that the first-order derivative of $f(t)$ at $t \in [t_{n-1}, t_n)$ is identical to $\dot{f}\left(\frac{t_{n-1}+t_n}{2}\right)$ for $n = 1, 2, \cdots, N$. Note that this simple rule guarantees the numerical integral f to be *non-decreasing* provided that $\dot{f} \geq 0$.

2.4 Hamiltonian Monte Carlo Algorithm

In Bayesian statistics, when the posterior distribution lacks a closed-form expression, a practical alternative is to approximate it through sampling. Markov Chain Monte Carlo (MCMC) methods (Liu, 2004) provide a well-established approach for drawing samples from a target distribution when direct sampling is infeasible but its density is known up to a normalization constant. The algorithm constructs a Markov chain of states by iteratively updating them one-by-one: in each iteration, a candidate sample is drawn from a predefined proposal distribution conditioned on the current state and accepted as a new state with a probability determined by the relative density of the proportional distribution. After a sufficient number of iterations (the burn-in phase), the most recent state of the chain is picked as a sample.

A major limitation of MCMC is the design of proposal distributions, which can significantly affect sampling efficiency, particularly in high-dimensional settings where variables exhibit strong correlations. If the logarithm of the proportional target density is differentiable, the Hamiltonian Monte Carlo (HMC) algorithm (Brooks et al., 2011) offers a more efficient alternative. HMC augments the sampling process by introducing auxiliary momentum variables and simulates their evolution using Hamiltonian dynamics, enabling more effective exploration of the target distribution. A detailed demonstration of its implementation can be found in (Gelman et al., 2013).

2.5 Stein Variational Gradient Descent

One practical drawback of HMC stems from its running time. That is, each Monte Carlo (MC) step in HMC requires dozens of leap-frog sub-steps, which slows down the algorithm significantly. Liu and Wang (2016) proposed a fast kernel density approximation algorithm, Stein Variational Gradient Descent (SVGD), that *deterministically* updates particles to match the target distribution. Because this algorithm does not require the leap-frog sub-steps, it is significantly faster than HMC. However,, the resulting approximation can be biased especially if the dimensionality of variables is high and the density kernel is ill-posed. Nonetheless, SVGD remains an efficient and practical approach for *initializing* samples prior to running HMC, substantially reducing the number of MC steps required during the burn-in phase.

https://doi.org/10.5194/egusphere-2026-2299
Preprint. Discussion started: 24 June 2026

3 Method

Our CIR process age inference method can be viewed as a multi-layer Bayesian hierarchical model. We first assume a CIR process prior on paths of the inverse sedimentation rates. Then, we convert each path to its corresponding age model through numerical integration with the midpoint rule. Finally, we compute the likelihood of proxy observations given the age model. In this section, we discuss explicit formulations of our modeling and its inference with mathematical equations. Throughout the section, we adhere to the following symbolic and notational conventions for a single sediment record.

- $Y = \{y_1, y_2, \cdots, y_N\}$ is a set of proxy observations of a sediment record.
- $V = \{v_1, v_2, \cdots, v_N\}$ is a set of proxy types of Y, e.g., benthic δ^{18}O or ^{14}C.
- $D = \{d_1, d_2, \cdots, d_N\}$ is the set of depths of the proxy observations in Y.
- $Z = \{z_1, z_2, \cdots, z_M\}$ is a set of M inducing depths that covers D.
- $A : \mathbb{R}_{\geq 0} \to \mathbb{R}$ is a random age-depth model function of the depth.
- $X : \mathbb{R}_{\geq 0} \to \mathbb{R}_{>0}$ is a random inverse sedimentation rate function of the depth.
- $\mathcal{F} = \left\{ f^{(k)} : \mathbb{R}_{\geq 0} \to \mathbb{R} \right\}_{k=1}^{K}$ is a set of independent random functions drawn from the OU-GP.
- $B \in \mathbb{R}$ is a scalar random variable that initializes the age model.

3.1 Model Formulation

With the above symbols together with three model parameters of the CIR process α, β and ρ, the full joint density function of our Bayesian modeling *given* α is formulated as follows:

$$p(Y, A_D, X_Z, B | V, \Theta, \alpha) = p(Y | V, A_D) \cdot p(A_D | X_Z, B) \cdot p(X_Z | \alpha, \Theta) \cdot p(B), \tag{5}$$

where α and $\Theta = \{\beta, \rho\}$ are parameters such that $\beta > 0$, $2\alpha \in \mathbb{N}$, and $\rho \in (0, 1)$.

First, $p(Y|A_D)$ is the likelihood of the proxy observations Y given their ages A_D. It has the following factorization:

$$p(Y | V, A_D) = \prod_{n=1}^{N} C_{v_n}(y_n | A(d_n)), \tag{6}$$

where C_v is the calibration model of proxy type v. Here we consider only two proxies, benthic δ^{18}O and ^{14}C.

For ^{14}C, we adapt a more robust distribution than the Gaussian, a generalized Student's t distribution (Christen and Pérez E, 2009), just as BIGMACS (Lee et al., 2023) and BACON (Blaauw and Christen, 2011), because ^{14}C proxy observations tend to be more involved with outliers due to contamination. That is, for a given ^{14}C calibration curve $\mu_{^{14}\mathrm{C}}$ and variance $\nu_{^{14}\mathrm{C}}$, we have:

$$C_{^{14}\mathrm{C}}(y_n | A(d_n)) \triangleq lst\left(y_n \middle| \mu_{^{14}\mathrm{C}}(A(d_n)) + \varrho_n, \frac{b_{^{14}\mathrm{C}}}{a_{^{14}\mathrm{C}}} \left(\nu_{^{14}\mathrm{C}}(A(d_n)) + \varsigma_n \right), 2 \cdot a_{^{14}\mathrm{C}} \right), \tag{7}$$

https://doi.org/10.5194/egusphere-2026-2299
Preprint. Discussion started: 24 June 2026

where ϱ_n and ς_n are the reservoir age and uncertainty aligned to y_n, respectively. Here, $lst\left(l, s^2, \nu\right)$ is the location-scale t distribution with a location l, scale s, and degree of freedom ν. $a_{^{14}\mathrm{C}}$ and $b_{^{14}\mathrm{C}}$ are hyperparameters in the generalized Student's t distribution, which can be specified by the users: Blaauw and Christen (2011) set $a_{^{14}\mathrm{C}} = 3$ and $b_{^{14}\mathrm{C}} = 4$ whereas Lee et al. (2023) choose $a_{^{14}\mathrm{C}} = 10$ and $b_{^{14}\mathrm{C}} = 11$, for example.

For benthic δ^{18}O, we assume that the stack is given a priori and each proxy observation has been standardized with respect to its record-specific shift and scale parameters (Lin et al., 2014; Ahn et al., 2017). Let μ_{stack} and ν_{stack} be the stack mean and variance functions of age. Then, we have:

$$C_{\delta^{18}\mathrm{O}}(y_n|A(d_n)) \triangleq \mathcal{N}(y_n|\mu_{stack}(A(d_n)), \nu_{stack}(A(d_n))), \tag{8}$$

or, if the model is to be more robust, then, just as ^{14}C, for hyperparameters $a_{\delta^{18}\mathrm{O}}$ and $b_{\delta^{18}\mathrm{O}}$ we have:

$$C_{\delta^{18}\mathrm{O}}(y_n|A(d_n)) \triangleq lst\left(y_n \middle| \mu_{stack}(A(d_n)), \frac{b_{\delta^{18}\mathrm{O}}}{a_{\delta^{18}\mathrm{O}}} \cdot \nu_{stack}(A(d_n)), 2 \cdot a_{\delta^{18}\mathrm{O}}\right). \tag{9}$$

Second, $p(A_D|X_Z, B)$ is the age model given the initial value B and inverse sedimentation rates X_Z at inducing depths in Z. As mentioned in Section 2.3, we use the numerical integration with the midpoint rule on X_Z to define A_D *deterministically*, i.e.,

$$A(d_n) = B + \sum_{m=1}^{j-1} (z_{m+1} - z_m) \cdot X(z_m) + \left(d_n - \frac{z_{j-1} + z_j}{2}\right) \cdot X(z_j), \quad d_n \in \left[\frac{z_{j-1} + z_j}{2}, \frac{z_j + z_{j+1}}{2}\right). \tag{10}$$

Clearly, if $d_n = (z_1 + z_2)/2$, then $A(d_n) = B$. One practical choice of the inducing depths in Z is to set z_1 and z_2 so that $d_1 = (z_1 + z_2)/2$ to make $A(d_1) = B$, that is, B is understood as the age at the first depth d_1. The other is to define $z_1 = -z_2$ that makes $A(0) = B$, i.e., B is the age at depth 0.

Third, $p(X_Z|\alpha, \Theta)$ is the inverse sedimentation rate model based on the CIR process, as demonstrated in Section 2.1.

$$p(X_Z|\alpha, \Theta) \triangleq \prod_{m=1}^{M-1} p(X(z_m)|X(z_{m+1}); \alpha, \Theta) \cdot p(X(z_M)|\alpha, \Theta), \tag{11}$$

where the CIR process is defined to go *backwards* in depths, as follows:

$$\begin{aligned} p(X(z_m)|X(z_{m+1}); \alpha, \Theta) \triangleq\ & \frac{\beta}{1 - \rho^{z_{m+1} - z_m}} \cdot \exp\left(-\frac{\beta}{1 - \rho^{z_{m+1} - z_m}} \left(\rho^{z_{m+1} - z_m} \cdot X(z_{m+1}) + X(z_m)\right)\right) \\ & \times \left(\frac{X(z_m)}{\rho^{z_{m+1} - z_m} \cdot X(z_{m+1})}\right)^{\frac{\alpha - 1}{2}} \cdot I_{\alpha - 1}\left(\frac{2\beta}{1 - \rho^{z_{m+1} - z_m}} \sqrt{\rho^{z_{m+1} - z_m} \cdot X(z_m) \cdot X(z_{m+1})}\right) \\ p(X(z_M)|\alpha, \Theta) \triangleq\ & Gamma(X(z_M)|\alpha, \beta) = \frac{\beta^\alpha}{\Gamma(\alpha)} \cdot X(z_M)^{\alpha - 1} \cdot \exp\left(-\beta \cdot X(z_M)\right). \end{aligned} \tag{12}$$

That is, we define the CIR process over *depths* (not time) just as BIGMACS and BACON.

Finally, $p(B) \propto 1_{B \geq \tau_0}(B)$ is a non-informative improper prior on the bias random variable B with the constraint of $B \geq \tau_0$ for a given lower bound τ_0 of $B = A\left((z_1 + z_2)/2\right)$. For example, if we set $d_1 = (z_1 + z_2)/2$, then τ_0 is the lower bound of age models at depth d_1; if we set $z_1 = -z_2$ so that $B = A(0)$, i.e., B is the age at depth 0, then τ_0 can be -0.1, because no sediment layer is younger than negative 0.1 kiloyears.

https://doi.org/10.5194/egusphere-2026-2299
Preprint. Discussion started: 24 June 2026

3.2 Inference

For the age inference, the CIR process that models the inverse sedimentation rates should be specified a priori. In other words, model parameters α and $\Theta = \{\beta, \rho\}$ are to be estimated from the data. Then, the age model is estimated given the specified CIR process. In the parameter estimation step, we run an expectation-maximization (EM) algorithm (Dempster et al., 1977) to iteratively update the parameters $\Theta = \{\beta, \rho\}$ given each α from its candidate set, and pick one which best fits to the criterion. In the age estimation step, after initialization by SVGD, we draw samples from the posterior of the age function by the HMC algorithm, *given* the model parameters. That is, just like BIGMACS (Lee et al., 2023), our algorithm returns the age model in the form of samples, not their single estimates only.

3.2.1 Parameter Estimation

To focus on the core idea, here we assume that model parameters are estimated from a single sediment record for convenience. As mentioned in Section 2.2, we only consider α such that $2\alpha \in \mathbb{N}$. Thus, the candidate set of α is $\{0.5, 1.0, 1.5, \cdots, K/2\}$ for some $K \in \mathbb{N}$ to make the set finite.

3.2.2 Estimation of Θ

We resort to an EM algorithm in parameter estimation of $\Theta = \Theta_\alpha$ for a given candidate α. One practical hurdle is that the posterior of $\mathrm{X_Z}$ given Y and parameters cannot be expressed in a closed-form distribution and its approximation via sampling is inefficient due to the modified Bessel function of the first kind of order $\alpha - 1$ in Equation (12), which is in nature hard to deal with in computation. To circumvent it, we instead consider a set of random functions $F = \left\{ f^{(k)} : \mathbb{R}_{\geq 0} \to \mathbb{R} \right\}_{k=1}^{K}$ where each random function $f^{(k)}$ follows the OU-GP prior, that is,

$$p(F_Z|\alpha, \Theta) \triangleq \prod_{k=1}^{2\alpha} \mathcal{N}\left(f_Z^{(k)} \middle| 0, \mathbb{H}_{ZZ} \right), \tag{13}$$

where $\mathbb{H}$ is an OU kernel defined as follows:

$$\mathbb{H}(t,s) \triangleq \exp\left(\frac{1}{2} \log \rho \cdot |t-s| \right) = \rho^{\frac{1}{2}|t-s|}. \tag{14}$$

By Section 2.2, one can restate $p(X_Z|\alpha, \Theta) = \mathbb{E}_{F_Z}[p(X_Z|F_Z; \alpha, \Theta) p(F_Z|\alpha, \Theta)]$ where:

$$p(X_Z|F_Z; \alpha, \Theta) \triangleq \prod_{m=1}^{M} 1_{X(z_m) = \frac{1}{2\beta} \sum_{k=1}^{2\alpha} \left(f^{(k)}(z_m) \right)^2} (X(z_m)). \tag{15}$$

Together with A_D, X_Z and B, we regard F_Z as another set of hidden variables in formulating an EM algorithm. For $i = 0, 1, 2, \cdots$, we iterate the following steps:

- (**E-step**) Given $\Theta_\alpha^{(i)} = \left\{ \beta^{(i)}, \rho^{(i)} \right\}$, we define the Q-function of Θ as follows:

$$\mathcal{Q}\left(\Theta \middle| \Theta_\alpha^{(i)} \right) \triangleq \mathbb{E}_{p\left(A_D, X_Z, F_Z, B \middle| Y, V; \Theta_\alpha^{(i)}, \alpha \right)} [\log p(Y, A_D, X_Z, F_Z, B | V; \Theta, \alpha)]. \tag{16}$$

https://doi.org/10.5194/egusphere-2026-2299
Preprint. Discussion started: 24 June 2026

– (**M-step**) We update $\Theta_\alpha^{(i+1)} = \mathrm{argmax}_\Theta \, \mathcal{Q}\left(\Theta \middle| \Theta_\alpha^{(i)}\right)$.

However, $p\left(A_D, X_Z, F_Z, B \middle| Y, V; \Theta^{(i)}, \alpha\right)$ is not expressed to be an exact and closed-form distribution. To circumvent it, we instead consider an empirical approximation of $\tilde{\mathcal{Q}}\left(\Theta \middle| \Theta_\alpha^{(i)}\right) \approx \mathcal{Q}\left(\Theta \middle| \Theta_\alpha^{(i)}\right)$ from the posterior samples of (A_D, X_Z, F_Z, B) given Y, V, $\Theta_\alpha^{(i)}$ and α, defined as follows:

$$\tilde{\mathcal{Q}}\left(\Theta \middle| \Theta_\alpha^{(i)}\right) \triangleq \frac{1}{L}\sum_{l=1}^{L} \log p\left(Y, A_D^{(l)}, X_Z^{(l)}, F_Z^{(l)}, B^{(l)} \middle| V; \Theta_\alpha^{(i)}, \alpha\right), \tag{17}$$

where $\left\{\left(A_D^{(l)}, X_Z^{(l)}, F_Z^{(l)}, B^{(l)}\right)\right\}_{l=1}^{L}$ is the set of independent and identically distributed samples drawn from $p\left(A_D, X_Z, F_Z, B \middle| Y, V; \Theta_\alpha^{(i)}, \alpha\right)$ by the SVGD and HMC algorithm.

3.2.3 Estimation of α

So far, we have discussed how to estimate parameters in $\Theta = \Theta_\alpha$ for a given α. What remains is a decision rule to choose α from a finite candidate set given their estimated parameters and the sediment record data. Rather than comparing their marginal likelihoods of the proxy values, we choose α by quantifying how "faithful" the marginal Gamma distribution of the inverse sedimentation rates is to the samples at depths where proxy observations are available for each α. To be specific, we compute the square of sample mean of the inverse sedimentation rate samples divided by their sample variance to calculate "empirical α from sub-samples" and compare it with "α given prior to running the EM algorithm", i.e., $\alpha \in \{0.5, 1.0, 1.5, \cdots, K/2\}$.

To summarize, we follow the below steps:

1. Estimating the parameters in $\hat{\Theta}_\alpha$ for each of $\alpha \in \{0.5, 1, 1.5, \cdots, K/2\}$ with some upper bound $K \in \mathbb{N}$
2. Evaluating $\mathcal{V}(\alpha) \triangleq |\alpha - \tilde{\alpha}|$ for an empirical $\tilde{\alpha} \triangleq \tilde{\mu}^2/\tilde{\sigma}^2$ where:

$$\tilde{\mu} \triangleq \frac{\sum_{l=1}^{L}\sum_{n=1}^{N} X^{(l)}(d_n)}{L \cdot N}, \qquad \tilde{\sigma}^2 \triangleq \frac{\sum_{l=1}^{L}\sum_{n=1}^{N} \left(X^{(l)}(d_n) - \tilde{\mu}\right)^2}{L \cdot N - 1} \tag{18}$$

3. Picking $\hat{\alpha} = \mathrm{argmin}_\alpha \, \mathcal{V}(\alpha)$ and the associated $\hat{\Theta}_{\hat{\alpha}}$

Here, each $X^{(l)}(d_n)$ is defined by $X^{(l)}(z_m)$ for the nearest z_m from d_n.

3.2.4 Age Estimation

Suppose that α and Θ have been estimated as $\hat{\alpha}$ and $\hat{\Theta}$, respectively. To estimate the age-depth model at a query depth $\tilde{d}$, we first draw samples from the posterior distribution $p\left(A_D, X_Z, F_Z, B \middle| Y, V; \hat{\Theta}, \hat{\alpha}\right)$ to get the set $\left\{X_Z^{(l)}, B^{(l)}\right\}_{l=1}^{L}$. Then, for each index $l = 1, 2, \cdots, L$, we compute the corresponding age-depth model sample $A^{(l)}\left(\tilde{d}\right)$ by the numerical integration with the midpoint rule, as follows:

$$A^{(l)}\left(\tilde{d}\right) = B^{(l)} + \sum_{m=1}^{j-1} (z_{m+1} - z_m) \cdot X(z_m) + \left(\tilde{d} - \frac{z_{j-1} + z_j}{2}\right) \cdot X(z_j), \quad \tilde{d} \in \left[\frac{z_{j-1} + z_j}{2}, \frac{z_j + z_{j+1}}{2}\right). \tag{19}$$

https://doi.org/10.5194/egusphere-2026-2299
Preprint. Discussion started: 24 June 2026

Finally, we have the posterior age-depth model samples $\left\{A^{(l)}\left(\tilde{d}\right)\right\}_{l=1}^{L}$ at a query depth $\tilde{d}$ to estimate its ages. More generally, one can estimate the age-depth model at a *set* of query depths $\tilde{D} = \left\{\tilde{d}_s\right\}_{s=1}^{S}$ by repeating the computation in Equation (19) at each $\tilde{d}_s$ for $s = 1, 2, \cdots, S$, given the *same* set $\left\{X_Z^{(l)}, B^{(l)}\right\}_{l=1}^{L}$ of the posterior samples – note that ages are autocorrelated over depths, and, for each $l = 1, 2, \cdots, L$, $A^{(l)}\left(\tilde{d}_s\right)$'s are systematically correlated because they are the functions of the identical $X_Z^{(l)}$ and $B^{(l)}$. By doing so, we can secure posterior sampled age-depth model *paths* rather than a set of individually drawn age-depth model samples.

3.3 CIR Process Age Inference Algorithm

So far, we have outlined the conceptual mathematical framework and inference method pertinent to a single sediment record. In practical applications, however, age-depth models are typically constructed using a set of parameters within published software packages, which in some cases are derived from curated sediment archives. To treat α, β, and ρ as *global* model parameters across multiple records, we introduce the notion of *standardized* inverse sedimentation rates, thereby ensuring cross-record compatibility. Specifically, each record is associated with a record-specific standardization parameter r, which rescales every depth $d \in D$ to d/r, and, correspondingly, each inducing depth $z \in Z$ to z/r, prior to the inference phase.

For reasons of identifiability, we standardized depths with respect to their corresponding ages such that, in the long-term average, the rate of change of depth with respect to age is approximately unity (i.e., a change of 1 standardized depth corresponds to approximately that of 1 kiloyear). This ensures a meaningful alignment across records and permits the application of a *globally-defined* CIR process to the rescaled inverse sedimentation rates. The standardization parameter r may either be specified a priori or treated as an estimable parameter within the inference framework. For instance, r might be defined as the ratio of the total depth range to the total age span – from the deepest to the shallowest sample – where the age-depth model is informed by prior belief, existing knowledge, point estimates derived from proxy data, or, in a more dynamic setting, by age estimates updated periodically during the execution of the EM algorithm.

Moreover, the use of certain proxies necessitates additional preprocessing steps. For instance, measurements of benthic $\delta^{18}O$ from individual sediment records must be standardized – accounting for record-specific shift and scale parameters – before alignment to the stack. This standardization may be informed by prior specifications or incorporated as part of the age estimation phase, allowing the shift and scale parameters to be estimated concurrently with the age-depth relationship.

In conjunction with addressing the aforementioned practical considerations, we formalize the age inference method within the CIR process framework, presenting two complementary algorithms derived from the model specification and inference strategy: one for parameter estimation and the other for age estimation. These are set forth as Algorithm A1 and Algorithm A2, respectively, together with full algorithmic details, including implementation specifics and computational considerations, in Appendix A.

https://doi.org/10.5194/egusphere-2026-2299
Preprint. Discussion started: 24 June 2026

4 Training Dataset

We consider radiocarbon dated cores from both the World Atlas of Late Quaternary Foraminiferal Oxygen and Carbon Isotopes (Mulitza et al., 2022) and the set of cores used by Lin et al. (2014). The Marine20 calibration curve, which we use for radiocarbon calibration, was developed for the non-polar ocean, defined as between $40°$S and $50°$N in the Atlantic and between $40°$S and $40°$N elsewhere (Heaton et al., 2020), hence we exclude cores outside of these boundaries. We also exclude cores from > $40°$N in the Atlantic Ocean due to temporally variable marine reservoir ages (Thornalley et al., 2011; Stern and Lisiecki, 2013; Lisiecki et al., 2022). We exclude any cores shallower than 1000 meters. We also only use cores with relatively high average SRs (SR > 8cm/kyr) to reduce the impact of smoothing by bioturbation. Only radiocarbon measurements from planktonic foraminifera are used, and cores must have at least four suitable radiocarbon ages to be included in the dataset. These selection criteria are very similar to those used by Lin et al. (2014) and Lee et al. (2023), but with stricter latitudinal boundaries. In total, there are 79 cores with 1133 radiocarbon proxy observations in the training dataset: see Appendix B for details regarding their locations, depths and references.

5 Results

In this section, we first present multiple estimates of the model parameters $\{\beta, \rho\}$ obtained via Algorithm A1 across a range of α values, and subsequently determine an appropriate choice of α from the set of candidates. We further assess the consistency of the proposed method by repeating the analysis over inducing depth sets Z's constructed at varying resolutions. Finally, for the purpose of benchmarking against BIGMACS, we infer the age models of four sediment records that were not used in the parameter estimation procedure, employing Algorithm A2.

5.1 Model Parameter Estimation

To employ the CIR-process-based age inference algorithm for estimating age-depth models, we first calibrate its model parameters, namely α, β, and ρ, using the training dataset described in Section 4. Specifically, we begin by running BIGMACS on the 79 sediment records, augmenting each record with an additional depth of 0 so that any age model sample at depth 0 is not below -0.1 kiloyear. For each record $p = 1, 2, \cdots, 79$, we estimate the record-specific standardization parameter r_p as the median of the mean sedimentation rates computed from the posterior samples. These parameters are then held fixed throughout the subsequent model parameter estimation phase.

Given that only the ^{14}C proxy is available in the training dataset as well, the step 'update record-specific parameters' in Algorithm A1 is omitted. For the calibration of ^{14}C measurements in the training records, we adopt the Marine20 calibration curve (Heaton et al., 2020). The likelihood function for the ^{14}C proxy observations is specified by Equation (7), with $a_{^{14}\mathrm{C}} = 3$ and $b_{^{14}\mathrm{C}} = 4$, consistent with (Blaauw and Christen, 2011).

For α, we consider the candidate set $\{0.5, 1.0, 1.5, 2.0, 2.5, 3.0\}$. To assess the robustness of the proposed algorithm, each dimensionless *standardized* inducing depth set $Z^{(p)}$ (with respect to the *fixed* record-specific standardization parameters) is

https://doi.org/10.5194/egusphere-2026-2299
Preprint. Discussion started: 24 June 2026

constructed as a regularly-spaced depth grid with interval lengths drawn from $\{0.05, 0.1, 0.2, 0.5, 1.0, 2.0\}$. Consequently, the algorithm is executed under 36 distinct configurations corresponding to all combinations of α values and grid resolutions for Z.

For each configuration, the EM algorithm iterates between the E- and M-steps until the parameter estimates for β and ρ converge. The algorithm is then continued for an additional 7500 iterations, after which the final estimates are taken as the medians of the corresponding 7500 values. For the posterior approximation, the number of samples is set to $L = 100$. The resulting model parameter estimates are reported in Tables C1 and C2 for β and ρ, respectively.

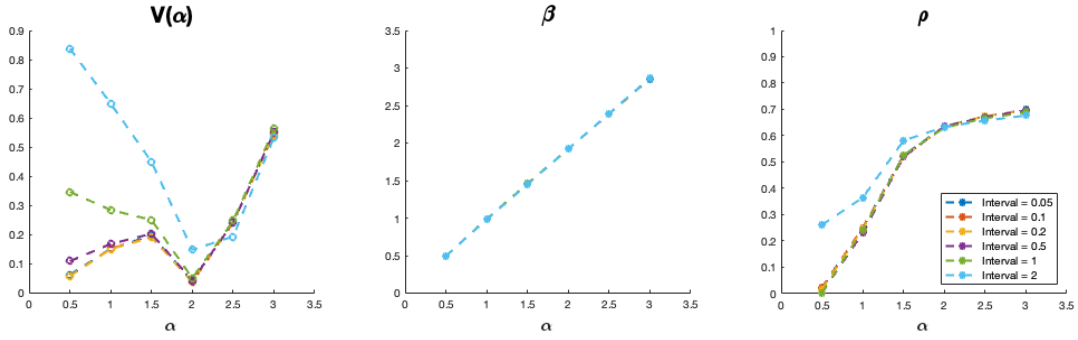

Figure 1. The first panel present five curves of $\mathcal{V}(\alpha)$ for various interval lengths. The second and third panels show the estimated β and ρ for candidates of α and various interval lengths, respectively.

For each grid resolution, $\hat{\alpha} = 2.0$ is selected according to the criterion described in Section 3.2.1; see Table C3 for the empirical values of $\tilde{\alpha}$ and the first panel of Figure 1 for the corresponding curves of $\mathcal{V}(\alpha)$ across different interval lengths. The second and third panels of Figure 1 present the results of the parameter estimation.

Overall, the estimates of β and ρ remain stable across different choices of α and interval lengths up to 1.0, but become inconsistent for larger intervals. This behavior is expected, as the sedimentation rate model is based on the CIR process, which is a consistent stochastic process, and so as its finite approximations defined on the discretizations of which the interval length is sufficiently small. Consequently, in implementing the EM algorithm, the inducding depth set Z may be fixed provided that the interval length of the rescaled Z – with respect to the updated record-specific standardization parameter – lies within the range 0.05 to 1.0.

Since the record-specific standardization parameter is defined as the median of the average sedimentation rates, it is not surprising that the estimated values of β are close to the corresponding α. Given that the estimates of β and ρ for $\alpha = 2.0$ remain stable up to an interval length of 1.0, we adopt the final parameter estimates $\hat{\beta} = 1.922$ and $\hat{\rho} = 0.634$. Although $\mathcal{V}(0.5)$ is nearly identical to – albeit marginally greater than – $\mathcal{V}(2.0)$ for certain interval lengths, the corresponding estimate of ρ is close to zero. This would imply that sedimentation rates exhibit virtually no autocorrelation with respect to depth, a conclusion which contradicts established scientific understanding.

https://doi.org/10.5194/egusphere-2026-2299
Preprint. Discussion started: 24 June 2026

5.2 Application to the Real Examples

Using the estimated model parameters $\hat{\alpha} = 2.0$, $\hat{\beta} = 1.922$ and $\hat{\rho} = 0.634$, we apply Algorithm A2 to four deep northeastern Atlantic Ocean sediment records that were not included in the model parameter estimation phase. Table 1 summarizes their key characteristics, including geographical locations, depths, and relevant references. Whereas only the ^{14}C proxy was employed in Section 5.1, both ^{14}C and benthic δ^{18}O proxies are incorporated here for age estimation.

Core	Lat °N	Lon °E	Depth m	References
GIK13289-2	18.07	341.99	2485	Sarnthein et al. (1994)
MD95-2042	37.80	349.83	3146	Bard et al. (1989, 2004, 2013); Shackleton et al. (2000, 2004)
ODP658C	20.75	341.42	2273	deMenocal et al. (2000); Knaack and Sarnthein (2005)
GeoB9508-5	15.50	342.05	2384	Mulitza et al. (2008)

Table 1. Core locations and data citations for validation.

To facilitate comparison with BIGMACS, each record is aligned to the same benthic δ^{18}O stack (the DNEA Stack (Lee et al., 2023)) using identical hyperparameter values, namely $a_{^{14}\mathrm{C}} = 10$, $b_{^{14}\mathrm{C}} = 11$, $a_{\delta^{18}\mathrm{O}} = 3$ and $b_{\delta^{18}\mathrm{O}} = 4$, consistent with the default settings of BIGMACS. The record-specific parameters – the standardization parameter and the shift and scale parameters associated with benthic δ^{18}O – are, however, estimated separately for each record.

For each sediment record, the inducing depth set Z is constructed such that (1) the points $z_m \in Z$ are regularly spaced, and (2) the interval length of the standardized depths z_m/r's is approximately 0.25. To satisfy the latter condition, we initialize r as the median of the average sedimentation rates obtained from BIGMACS[2], and define Z so that $(z_{m+1} - z_m)/r \approx 0.25$ for each record.

Figure 2 presents a comparison of the age estimation results for GIK13289-2 obtained using the CIR process age inference algorithm and BIGMACS, respectively. The standardized interval length is 0.2395 with respect to the estimated standardization parameter. Specifically, the three panels on the left display the results produced by the proposed algorithm, whilst the three panels on the right present the corresponding results generated by BIGMACS.

Within each set of three panels, the first (A) depicts the posterior-sampled age-depth trajectories (black curves), together with their 95% credible bands (dashed curves) and posterior median (red curve). The blue bars represent the 95% credible intervals of the *individual* age estimates derived solely from the ^{14}C proxy. The second panel (B) displays the logarithms of the posterior sampled sedimentation rate trajectories (black curves), along with their 95% credible bands (dashed curves) and posterior median (red curve). Blue triangles mark the depths at which ^{14}C proxy observations are available. The third panel (C) illustrates the alignment of the benthic δ^{18}O proxy observations with the target stack (DNEA). Stars denote the posterior medians of the estimated age samples, and the horizontal bars indicate their corresponding 95% credible intervals. The dots and shaded gray region represent the mean and 95% credible band of the target stack, respectively.

[2]In practice, the initial value of r can be informed by prior knowledge of the sedimentation characteristics of the record under consideration.

https://doi.org/10.5194/egusphere-2026-2299
Preprint. Discussion started: 24 June 2026

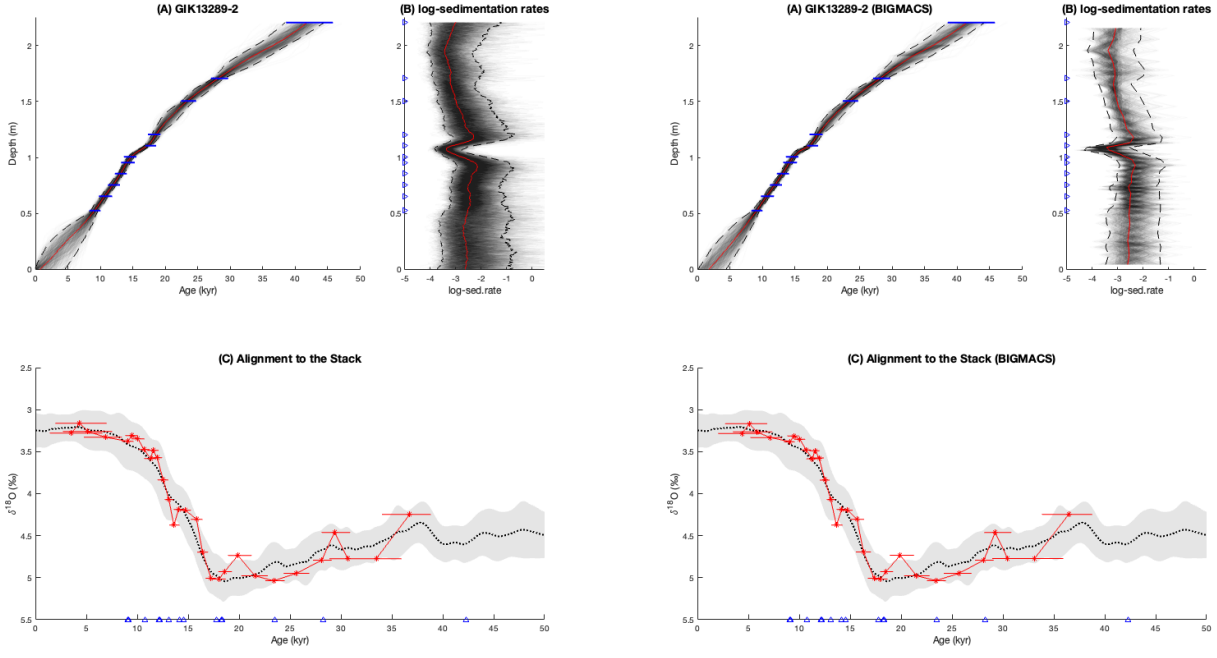

Figure 2. Age estimation results of GIK13289-2.

Whereas both the age estimates and the corresponding log-sedimentation rates are broadly consistent for GIK13289-2, a marked discrepancy in the log-sedimentation rates is observed for MD95-2042, particularly over the upper portion of the core (up to 17.2 meters), as shown in Figure 3. The standardized interval length for this record is 0.2565 with respect to the estimated standardized parameter.

The inferred age model produced by the proposed algorithm agrees closely with that of BIGMACS at depths where both proxies are available. However, divergence arises between 16 and 17.2 meters, where the ^{14}C proxy is absent and only benthic δ^{18}O proxy observations are available. This discrepancy is further illustrated in the third panels (C), which depict the alignment of benthic δ^{18}O observations to the target stack. In this interval, the proposed algorithm yields narrower posterior uncertainty for the age model than BIGMACS. Although the CIR-process-based sedimentation rate model imposes a more structured posterior distribution – resulting in comparatively tighter credible bands than those obtained from BIGMACS – this constraint promotes a more coherent alignment of benthic δ^{18}O observations with the target stack, rather than causing overfitting.

Figure 4 and 5 present the corresponding comparisons for the sediment records ODP658C and GeoB9508-5, for which the standardized interval lengths are 0.2309 and 0.2610, respectively. For both records, the age estimates are consistent between the two methods at depths where both proxies are available. However, as observed for MD95-2042, discrepancies emerge in

https://doi.org/10.5194/egusphere-2026-2299
Preprint. Discussion started: 24 June 2026

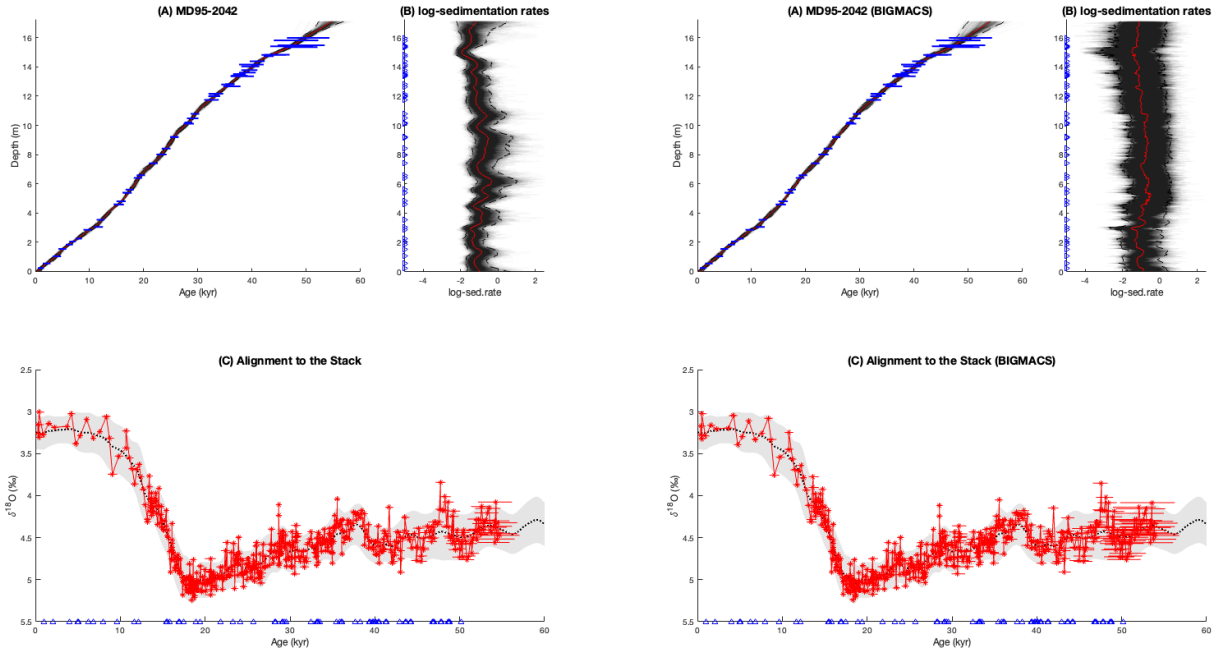

Figure 3. Age estimation results of MD95-2042 (up to 17.2 meters).

intervals where only the benthic δ^{18}O proxy is present. In addition, the inferred posterior sedimentation rate trajectories differ substantially between the two approaches in both cases.

More specifically, for ODP658C, the posterior sedimentation rate trajectories inferred by the proposed algorithm exhibit a consistent degree of smoothness across depths. In contrast, the trajectories produced by BIGMACS display smoothness that varies with the resolution of the proxy observations. This difference arises because, in BIGMACS, sedimentation rate modeling is performed separately within intervals defined by the availability of proxy observations, whereas the proposed method employs a consistent sedimentation rate model over depth based on the CIR process.

Furthermore, BIGMACS permits a subset of benthic δ^{18}O proxy observations to be aligned to the target stack beyond 35 kiloyears, despite the absence of observations that can be matched to the prominent peak of the stack between 35 and 40 kiloyears. By contrast, the proposed algorithm constrains the alignment to within 35 kiloyears, thereby avoiding such extrapolative behavior.

For GeoB9508-5, the benthic δ^{18}O proxy observations beyond 6 meters are, under both algorithms, predominantly aligned to a relatively flat – and therefore less informative – segment of the target stack, despite exhibiting a subtle yet discernible periodic pattern. The logarithms of the sedimentation rate trajectories inferred by BIGMACS are nearly vertical, rendering them effectively uninformative and leading to more ambiguous alignments than those obtained from the proposed algorithm. For

https://doi.org/10.5194/egusphere-2026-2299
Preprint. Discussion started: 24 June 2026

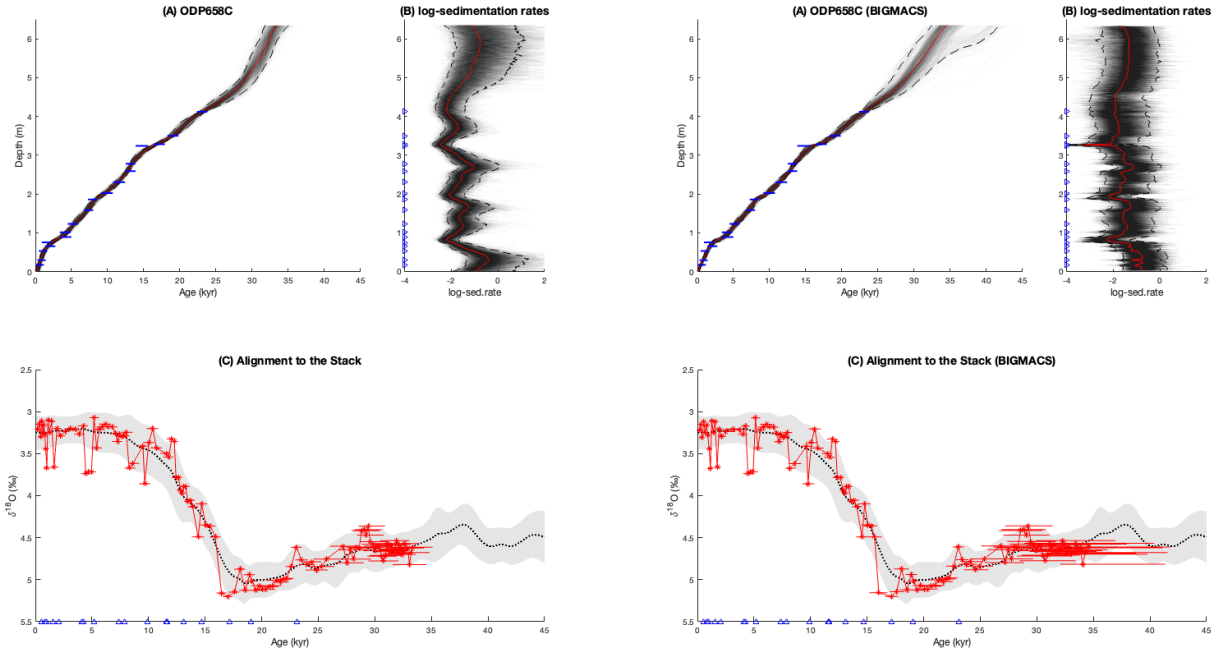

Figure 4. Age estimation results of ODP658C.

instance, the deepest benthic δ^{18}O observations may be aligned by BIGMACS to the stack peak at approximately 54 kiloyears, whereas the proposed method predominantly constrains their alignment to the subsequent peak at around 59 kiloyears.

To examine the sensitivity of the proposed algorithm to the choice of interval lengths of the inducing depth set Z, we implement it using grid resolutions of approximately 1.0, 0.5, 0.25, and 0.125 after applying standardization parameters, and present the corresponding comparisons in Appendix C. The results for GIK13289-2, MD95-2042, ODP658C, and GeoB9508-5 are shown in Figures C1, C2, C3, and C4, respectively. Across all four sediment records, the inferred age models remain consistent over the range of grid resolutions considered, indicating that the proposed algorithm is robust with respect to the choice of interval length, even when the standardized interval length is as large as approximately 1.0.

6 Discussion

Our proposed CIR Process Age Inference algorithm offers several advantages over BIGMACS. First, it models inverse sedimentation rates as a continuous and coherent stochastic process – specifically, the CIR process – yielding posterior sedimentation rates that exhibit consistent smoothness across depth. In contrast, BIGMACS relies on a discrete AR formulation, which introduces resolution-dependent smoothing; as a result, the inferred age-depth relationship may lack robustness, varying significantly with the inclusion or exclusion of specific depth points. Second, although our model adopts a more tightly

https://doi.org/10.5194/egusphere-2026-2299
Preprint. Discussion started: 24 June 2026

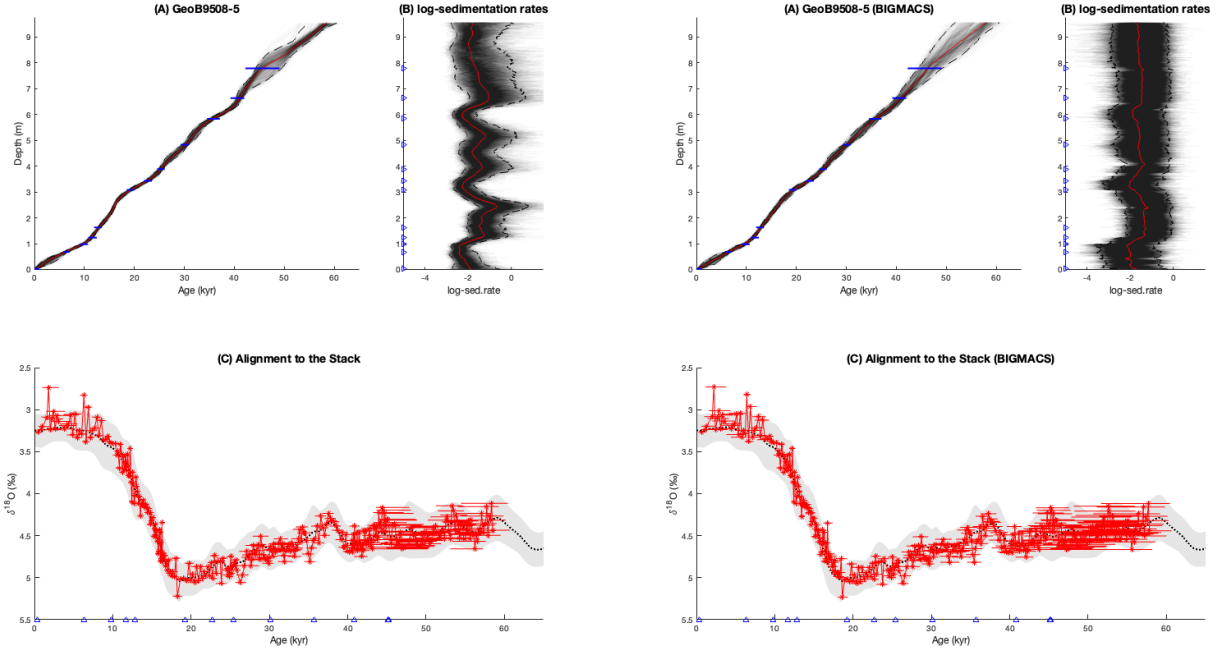

Figure 5. Age estimation results of GeoB9508-5.

constrained prior – yielding narrower credible intervals for individual sedimentation rates and raising concerns about overfit to the training data – this regularization in fact promotes more faithful alignment of indirect proxy observations with prominent features in the reference stack. This suggests that the CIR-based formulation of inverse sedimentation rates is more physically and statistically coherent than the first-order AR approach employed in BIGMACS. Third, the integration of SVGD with HMC in our inference framework proves more robust in practice than the particle smoothing and MCMC scheme used in BIGMACS. Indeed, the latter sometimes encounters errors unless depth ages are carefully initialized or supplemented with auxiliary age constraints. In contrast, our algorithm demonstrates reliable performance provided the record-specific standardization parameter is reasonably well specified.

Notwithstanding its advantages, our proposed algorithm presents several limitations that warrant attention in future work. First, the computational complexity of the baseline implementation scales cubically with the size of the inducing depth set Z – the depths at which inverse sedimentation rates are sampled – rendering it impractical for large datasets. As discussed in Appendix A, a substantial improvement can be achieved by spacing the elements of Z regularly, which reduces the time complexity to linear in $|Z|$. While this is a simple yet effective modification, the overall computational burden remains proportional to $|Z| \times |D|$, where D denotes the set of depths at which proxy observations are recorded – a cost not incurred by BIGMACS. When combined with HMC, which is inherently slower than the MCMC scheme used in BIGMACS, this results in a significantly longer runtime.

https://doi.org/10.5194/egusphere-2026-2299
Preprint. Discussion started: 24 June 2026

For instance, generating the results for the four real-world case studies in Section 5.2 with a spacing interval of approximately 0.5 units takes over an hour, comparing to under 20 minutes for BIGMACS.

Second, the estimated model parameter $\hat{\rho} = 0.634$, derived in Section 5.1, implies that the autocorrelation of inverse sedimentation rates decays below 0.01 (and 0.001) at standardized depth intervals exceeding 10.1 (and 15.1, respectively). Given that standardization is designed such that depth approximately tracks age under a unit sedimentation rate (one per one kiloyear), this corresponds to a temporal autocorrelation range up to approximately 10.1 (or 15.1) kiloyears. In practical terms, the model assumes that sedimentation dynamics at observations separated by more than these boundaries are nearly independent – a reasonable assumption for records spanning the Late Pleistocene and Holocene, but potentially limiting when applied to longer, sparser cores extending over multiple glacial cycles or on million-year timescales. The current parameterization, trained on a radiocarbon-calibrated dataset dominated by the past 50 kiloyears, inherently reflects the climate structure of this period – characterized by the warm Holocene (0–10 kyr BP), rapid deglaciation (10–18 kyr BP), and Last Glacial Maximum (18–28 kyr BP). The autocorrelation timescale of less than 10 kiloyears likely emerges from the pacing of these climate transitions, which are themselves governed by Earth's astronomical cycles, with dominant periodicities ranging from approximately 20–400 kiloyears. However, the relative influence of these cycles has varied across geological time, suggesting that sedimentation dynamics on longer timescales may exhibit different memory structures. While the incorporation of autocorrelated sedimentation rates improves model reliability – based on the theory that climate-driven sediment supply is itself temporally persistent – future work should aim to estimate such autocorrelation directly from sediment records across diverse timescales. This would enable the development of more adaptable, era-specific models, thereby extending the applicability of our framework beyond the Late Pleistocene and Holocene epochs to deeper time.

From a scientific perspective, our proposed algorithm improves the marine sedimentary chronology near the limits of radiocarbon dating, leading to more accurate age modeling for many paleoclimate events such as Heinrich event 4 (HE4; 38 ka) (Hemming, 2004), HE5 (45 ka), HE5a (~50 ka) (Rashid et al., 2003), HE6 (60 ka), HQ (68 ka) (Bassis et al., 2017; Zhou et al., 2021), and Marine Isotope Stage 4 (MIS 4; 60-70 ka). In particular, previous research indicates that the ice-sheet extent during MIS 4 could be similar to that of the Last Glacial Maximum (Doughty et al., 2021; McCarthy et al., 2008; Seidenkrantz et al., 2019), whereas data from sediment cores suggest a more modest ice volume change (Spratt and Lisiecki, 2016). Better age estimates for high-quality paleoceanographic records during this period, which the proposed algorithm can help produce, may help resolve the source of this apparent amplitude mismatch. Additionally, the Laschamp geomagnetic excursion occurred during this period (41 ka) (Channell et al., 2020; Singer, 2014). While this geomagnetic event has been dated by $^{40}Ar/^{39}Ar$ measurements, a recent study suggests it caused "a global environmental crisis" (Cooper et al., 2021). This controversial proposal (Hawks, 2021; Picin et al., 2021) can be tested by environmental reconstructions from marine sediments, and the improved chronology resulting from the proposed algorithm will aid investigations into this topic.

https://doi.org/10.5194/egusphere-2026-2299
Preprint. Discussion started: 24 June 2026

7 Conclusion

Accurate dating of sediment records is a cornerstone of paleoclimatology and paleoceanography, underpinning the reconstruction of past climate dynamics and the synchronization of global environmental change. While existing methods have advanced the integration of direct and indirect age proxies and the regularization of inferred age-depth modeling, they remain subject to certain limitations – particularly in terms of model consistency and robustness on the sedimentation rates. In this study, we introduce a novel age estimation algorithm within a hierarchical Bayesian framework, designed to address key shortcomings of established algorithms such as BACON and BIGMACS. Our method centers on a principled model of inverse sedimentation rates, formulated via the Cox-Ingersoll-Ross (CIR) process and trained on a carefully curated set of 79 sediment records. Through validation on four real-world cores, we demonstrate that the resulting age-depth models exhibit greater consistency and robustness compared to those produced by BIGMACS, particularly in preserving smoothness of posterior sedimentation rates and avoiding alignment artifacts.

That said, the current implementation entails notable computational costs, with inference times exceeding those of BIGMACS due to the excessive time complexity of the CIR-process-based model and the use of Hamiltonian Monte Carlo. Moreover, our trained sedimentation model is not readily transferable to million-year-scale archives without re-estimation of parameters. To address these limitations, we are pursuing a more efficient computational implementation, transitioning from CPU-based to GPU-accelerated computation, to exploit parallelism inherent in the underlying matrix multiplications. Furthermore, while the present algorithm replaces only the age-depth model component of BIGMACS, we intend to extend our framework to encompass and improve upon the stacking procedure as well – rendering it both mathematically more rigorous and computationally more efficient. A particular challenge lies in the assumption of homogeneity across input records, which may not hold in practice. We are therefore exploring a new hierarchical modeling approach capable of automatically identifying and classifying potentially heterogeneous cores, thereby enhancing the adaptability and reliability of the overall age-depth modeling and stacking pipeline.

https://doi.org/10.5194/egusphere-2026-2299
Preprint. Discussion started: 24 June 2026

Appendix A: Details of Section 3.3

In Section 3.1, we stated the model for a *single* record. To estimate the CIR process model parameters, however, we might need to consider *multiple* records. Here, we assume to process P sediment records as the training data, and each record p of size $N^{(p)}$ is involved with the symbols of $\left\{Y^{(p)}, V^{(p)}, D^{(p)}, Z^{(p)}, A^{(p)}, X^{(p)}, F^{(p)}, B^{(p)}\right\}$ for $p = 1, 2, \cdots, P$, and let $\mathrm{Y} = \left\{Y^{(p)}\right\}_{p=1}^{P}$, $\mathrm{V} = \left\{V^{(p)}\right\}_{p=1}^{P}$ and so on. Each inducing depth set $Z^{(p)}$ is defined to cover $D^{(p)}$, and, for notational simplicity, we assume that each $\left(D^{(p)}, Z^{(p)}\right)$ have already been rescaled by the record-specific standardization parameter r_p by $\left(D^{(p)}, Z^{(p)}\right) \to \left(D^{(p)}/r_p, Z^{(p)}/r_p\right)$. With extended notations, we have the following full joint density function for formulation the EM algorithm:

$$p(\mathrm{Y}, \mathrm{A_D}, \mathrm{X_Z}, \mathrm{F_Z}, \mathrm{B} | \mathrm{V}, \Theta, \alpha) = p(\mathrm{Y}|\mathrm{V}, \mathrm{A_D}) \cdot p(\mathrm{A_D}|\mathrm{X_Z}, \mathrm{B}) \cdot p(\mathrm{X_Z}|\mathrm{F_Z}, \alpha, \Theta) \cdot p(\mathrm{F_Z}|\alpha, \Theta) \cdot p(\mathrm{B}) \tag{A1}$$

Factors of the above joint density function are defined straightforwardly as follows:

$$\begin{aligned} p(\mathrm{Y}|\mathrm{V}, \mathrm{A_D}) &= \prod_{p=1}^{P} p\left(Y^{(p)} \middle| V^{(p)}, A^{(p)}_{D^{(p)}}\right), \quad p(\mathrm{A_D}|\mathrm{X_Z}, \mathrm{B}) = \prod_{p=1}^{P} p\left(A^{(p)}_{D^{(p)}} \middle| X^{(p)}_{Z^{(p)}}, B^{(p)}\right), \\ p(\mathrm{X_Z}|\mathrm{F_Z}, \alpha, \Theta) &= \prod_{p=1}^{P} p\left(X^{(p)}_{Z^{(p)}} \middle| F^{(p)}_{Z^{(p)}}, \alpha, \Theta\right), \quad p(\mathrm{F_Z}|\alpha, \Theta) = \prod_{p=1}^{P} p\left(F^{(p)}_{Z^{(p)}} \middle| \alpha, \Theta\right), \quad p(\mathrm{B}) = \prod_{p=1}^{P} p\left(B^{(p)}\right), \end{aligned} \tag{A2}$$

where each component is defined as Section 3.1 and 3.2.1.

The corresponding EM algorithm is extended as below. For $i = 0, 1, 2, \cdots$, we iterate the following steps:

- (**E-step**) Given $\Theta^{(i)}_{\alpha} = \left\{\beta^{(i)}, \rho^{(i)}\right\}$, we define the Q-function of Θ as follows:

$$\mathcal{Q}\left(\Theta \middle| \Theta^{(i)}_{\alpha}\right) \triangleq \mathbb{E}_{p\left(\mathrm{A_D}, \mathrm{X_Z}, \mathrm{F_Z}, \mathrm{B} \middle| \mathrm{Y}, \mathrm{V}; \Theta^{(i)}_{\alpha}, \alpha\right)} [\log p(\mathrm{Y}, \mathrm{A_D}, \mathrm{X_Z}, \mathrm{F_Z}, \mathrm{B} | \mathrm{V}; \Theta, \alpha)]. \tag{A3}$$

- (**M-step**) We update $\Theta^{(i+1)}_{\alpha} = \mathrm{argmax}_{\Theta}\, \mathcal{Q}\left(\Theta \middle| \Theta^{(i)}_{\alpha}\right)$.

Because

$$\mathcal{Q}\left(\Theta \middle| \Theta^{(i)}_{\alpha}\right) = \sum_{p=1}^{P} \mathbb{E}_{p\left(A^{(p)}_{D^{(p)}}, X^{(p)}_{Z^{(p)}}, \mathcal{F}^{(p)}_{Z^{(p)}}, B^{(p)} \middle| Y^{(p)}, V^{(p)}; \Theta^{(i)}_{\alpha}, \alpha\right)} \left[\log p\left(Y^{(p)}, A^{(p)}_{D^{(p)}}, X^{(p)}_{Z^{(p)}}, \mathcal{F}^{(p)}_{Z^{(p)}}, B^{(p)} \middle| V^{(p)}; \Theta, \alpha\right)\right], \tag{A4}$$

the approximated Q-function analogous to Equation (17) is represented as follows:

$$\tilde{\mathcal{Q}}\left(\Theta \middle| \Theta^{(i)}_{\alpha}\right) \triangleq \frac{1}{L} \sum_{l=1}^{L} \sum_{p=1}^{P} \log p\left(Y^{(p)}, A^{(p,l)}_{D^{(p)}}, X^{(p,l)}_{Z^{(p)}}, F^{(p,l)}_{Z^{(p)}}, B^{(p,l)} \middle| V^{(p)}, \Theta, \alpha\right), \tag{A5}$$

where $\left\{\left(A^{(p,l)}_{D^{(p)}}, X^{(p,l)}_{Z^{(p)}}, F^{(p,l)}_{Z^{(p)}}, B^{(p,l)}\right)\right\}_{l=1}^{L}$ is the set of independent and identically distributed samples drawn from $p\left(A^{(p)}_{D^{(p)}}, X^{(p)}_{Z^{(p)}}, F^{(p)}_{Z^{(p)}}, B^{(p)} \middle| Y^{(p)}, V^{(p)}; \Theta^{(i)}_{\alpha}, \alpha\right)$ by the SVGD and HMC algorithm.

Here are some details of the implementation. As Equations (10) and (15), $\mathrm{A_D}$ and $\mathrm{X_Z}$ are deterministic functions of $\mathcal{F}_{\mathrm{Z}}$ and B. Thus, once each pair $\left(F^{(p,l)}_{Z^{(p)}}, B^{(p,l)}\right)$ is sampled from the marginal posterior $p\left(F^{(p)}_{Z^{(p)}}, B^{(p)} \middle| Y^{(p)}, V^{(p)}; \Theta^{(i)}_{\alpha}, \alpha\right)$,

https://doi.org/10.5194/egusphere-2026-2299
Preprint. Discussion started: 24 June 2026

the corresponding $A_D^{(p,l)}$ and $X_{Z^{(p)}}^{(p,l)}$ are promptly determined. Since the logarithm of the marginal joint density function $p\left(Y^{(p)}, F_{Z^{(p)}}^{(p)}, B^{(p)} \middle| V^{(p)}; \Theta, \alpha\right)$ is differentiable with respect to each hidden variable $f_{Z^{(p)}}^{(k,p)} \in F_{Z^{(p)}}^{(p)}$, $B^{(p)}$, and each parameter in Θ, an efficient SVGD and HMC algorithms are available in drawing posterior samples of $\left(F_{Z^{(p)}}^{(p,l)}, B^{(p,l)}\right)$, as discussed in Sections 2.4 and 2.5. To be specific, the numerical integration with the midpoint rule guarantees the monotonicity of the integral if the first-order derivatives are all nonnegative, as discussed in Section 2.3, which means that the fundamental assumption – the deeper is the older – is automatically fulfilled.

Moreover, $\mathbb{H}_{ZZ}$ in Equation (14) is a $M \times M$ Toeplitz correlation matrix if inducing depths in Z are spaced regularly, so its inverse and Cholesky decomposition are given as exact and closed-form matrices in the time complexity *linear* to M (Golub and Van Loan, 2013), which means that increasing M does not significantly slow down the computation in the SVGD and HMC algorithms, i.e., not cubic but linear. Finally, the constraint on $B \geq \tau_0$ can be easily obtained by the reparameterization $B \triangleq b^2 + \tau_0$ for a scalar random variable b.

The time complexity of posterior sampling is linear to the number of samples L. A more efficient approximation of the Q-function can be achieved by the randomly shifted lattice rule (L'Ecuyer et al., 2010), which slightly "perturbs" $Z^{(p)}$ for each sample $l = 1, 2, \cdots, L$. To be specific, each $Z^{(p,l)}$ is derived by adding a very small random number ϵ_l to each element of $Z^{(p)}$ so that it still covers $D^{(p)}$. By doing so, the age model is computed by:

$$\begin{aligned} A^{(p,l)}(d) = B^{(p,l)} + \epsilon_l \cdot X^{(p,l)}\left(z_1^{(p)} + \epsilon_l\right) + \sum_{m=1}^{j-1} \left(z_{m+1}^{(p)} - z_m^{(p)}\right) \cdot X^{(p,l)}\left(z_m^{(p)} + \epsilon_l\right) \\ + \left(d - \frac{z_{j-1}^{(p)} + z_j^{(p)}}{2} - \epsilon_l\right) \cdot X^{(p,l)}\left(z_j^{(p)} + \epsilon_l\right), \quad d \in \left[\frac{z_{j-1}^{(p)} + z_j^{(p)}}{2} + \epsilon_l, \frac{z_j^{(p)} + z_{j+1}^{(p)}}{2} + \epsilon_l\right). \end{aligned} \tag{A6}$$

The above EM algorithm has been specified under the assumption that the record-specific standardization parameters and any other parameters included in the likelihood of the proxy observations are given a priori. If they are not given a priori but to be estimated (or tuned) as well, then we iterate the following steps, just like the age estimation algorithm in BIGMACS.

1. Given the record-specific standardization parameters and those of likelihood of the proxy observations, we draw posterior samples of the age-depth models, inverse sedimentation rates, GP random functions, and bias random variables.

2. Given the posterior samples of the age-depth models, inverse sedimentation rates, GP random functions, and bias random variables, we compute the approximation of the Q-function as Equation (A5) and update the tuple of model parameters α, β and ρ as its maximizer.

3. Given the associated age-depth model samples of the record, we update the record-specific standardization parameters and those of likelihood of the proxy observations.

For example, one can update each record-specific standardization parameter as the median of average sedimentation rates of L posterior samples:

https://doi.org/10.5194/egusphere-2026-2299
Preprint. Discussion started: 24 June 2026

$$r_p = median\left(\left\{\frac{d_N - d_1}{A^{(p,l)}(d_N) - A^{(p,l)}(d_1)}\right\}_{l=1}^{L}\right), \quad p = 1, 2, \cdots, P. \tag{A7}$$

Updating parameters of proxy likelihood relies on the nature of proxy. While ^{14}C calibration model does not have such parameters, one needs to specify the record-specific shift and scale parameters of the benthic δ^{18}O proxy to align each record to the stack. Suppose that h_p and s_p are the shift and scale parameters of the sediment record p. Then, the likelihood of the *raw* benthic δ^{18}O proxy observation $y_n^{(p)}$ of Equation (8) is redefined as below:

$$C_{\delta^{18}\mathrm{O}}(y_n|A(d_n)) \triangleq \mathcal{N}\big(y_n\big|h_p + s_p \cdot \mu_{stack}(A(d_n)), s_p^2 \cdot \nu_{stack}(A(d_n))\big), \tag{A8}$$

and, the objective function to estimate h_p and s_p can be defined by:

$$\mathcal{L}(h_p, s_p) \triangleq \frac{1}{L}\sum_{l=1}^{L} \log \mathcal{N}\Big(y_n\Big|h_p + s_p \cdot \mu_{stack}\Big(A^{(p,l)}(d_n)\Big), s_p^2 \cdot \nu_{stack}\Big(A^{(p,l)}(d_n)\Big)\Big). \tag{A9}$$

That is, given posterior samples of age-depth models, one can update the shift and scale parameters that maximize the above objective function by gradient ascent for each p.

For estimating α, similar to Section 3.2.1, one can follow the below steps:

1. Estimating the parameters in $\hat{\Theta}_\alpha$ for each of $\alpha \in \{0.5, 1, 1.5, \cdots, K/2\}$ with some upper bound $K \in \mathbb{N}$
2. Let $\mathcal{V}(\alpha) \triangleq |\alpha - \tilde{\alpha}|$ for an empirical $\tilde{\alpha} \triangleq \tilde{\mu}^2/\tilde{\sigma}^2$ where:

$$\tilde{\mu} \triangleq \frac{\sum_{l=1}^{L}\sum_{p=1}^{P}\sum_{n=1}^{N_p} X^{(p,l)}\left(d_n^{(p)}\right)}{L \cdot \sum_{p=1}^{P} N_p}, \qquad \tilde{\sigma}^2 \triangleq \frac{\sum_{l=1}^{L}\sum_{p=1}^{P}\sum_{n=1}^{N_p}\left(X^{(p,l)}\left(d_n^{(p)}\right) - \tilde{\mu}\right)^2}{L \cdot \sum_{p=1}^{P} N_p - 1}. \tag{A10}$$

3. Picking $\hat{\alpha} = \mathrm{argmin}_\alpha \mathcal{V}(\alpha)$ and the associated $\hat{\Theta}_{\hat{\alpha}}$

Here, each $X^{(p,l)}\left(d_n^{(p)}\right)$ is defined by $X^{(p,l)}\left(z_m^{(p)}\right)$ for the nearest $z_m^{(p)}$ from $d_n^{(p)}$.

After estimating all the CIR process model parameters α, β and ρ, one can estimate the age model of an arbitrary sediment record by iterating the following two steps:

1. Given the record-specific standardization parameters and those of likelihood of the proxy observations, we draw posterior samples of the age-depth models, inverse sedimentation rates, GP random functions, and bias random variables.
2. Given the associated age-depth model samples of the record, we update the record-specific standardization parameters and those of likelihood of the proxy observations.

What we have discussed so far are organized into the CIR process age inference algorithms, which can be found in the main manuscript: see Algorithm A1 and Algorithm A2.

https://doi.org/10.5194/egusphere-2026-2299
Preprint. Discussion started: 24 June 2026

Algorithm A1 CIR Process Age Inference (Parameter Estimation)

for $k = 1, 2, \cdots, K$ **do**
  define $\alpha = k/2$.
  initialize the sets of model parameters $\Theta_\alpha = \Theta_\alpha^{(0)}$ and record-specific parameters.
  while convergence **do**
    for records $p = 1, 2, \cdots, P$ **do**
      rescale depths $D^{(p)}$ and $Z^{(p)}$ with respect to the record-specific standardization parameter.
      rescale proxy observations $Y^{(p)}$ with respect to the record-specific parameters (if needed).
      for samples $l = 1, 2, \cdots, L$ **do**
        initialize $\left(F_{Z^{(p)}}^{(p,l)}, B^{(p,l)}\right)$'s by SVGD.
        draw $\left(F_{Z^{(p)}}^{(p,l)}, B^{(p,l)}\right) \sim_{i.i.d.} p\left(F_{Z^{(p)}}, B^{(p)} \middle| Y^{(p)}, V^{(p)}, \Theta_\alpha^{(r)}, \alpha\right)$ by HMC.
        compute $X_{Z^{(p)}}^{(p,l)}$ and $A_{D^{(p)}}^{(p,l)}$ given $F_{Z^{(p)}}^{(p,l)}$ and $B^{(p,l)}$.
      end for
    end for
    update $\Theta_\alpha^{(i+1)} = \text{argmax}_{\Theta_\alpha} \tilde{\mathcal{Q}}\left(\Theta_\alpha \middle| \Theta_\alpha^{(i)}\right)$ defined in Equation (A5) by gradient ascent.
    update record-specific parameters.
  end while
  compute $\mathcal{V}(\alpha) = |\alpha - \tilde{\alpha}|$ by Equation (A10).
end for
choose $\hat{\alpha} = \text{argmin}_\alpha \mathcal{V}(\alpha)$ and $\hat{\Theta} = \hat{\Theta}_{\hat{\alpha}}$.

Algorithm A2 CIR Process Age Inference (Age Estimation)

initialize the record-specific parameters.
while convergence **do**
  rescale depths $D^{(p)}$ and $Z^{(p)}$ with respect to the record-specific standardization parameter.
  rescale proxy observations $Y^{(p)}$ with respect to the record-specific parameters (if needed).
  for $l = 1, 2, \cdots, L$ **do**
    initialize $\left(F_Z^{(l)}, B^{(l)}\right)$'s by SVGD.
    draw $\left(F_Z^{(l)}, B^{(l)}\right) \sim_{i.i.d.} p\left(F_Z, B \middle| Y, P, \hat{\Theta}_{\hat{\alpha}}, \hat{\alpha}\right)$ by HMC.
    compute $X_Z^{(l)}$ and $A_D^{(l)}$ given $F_Z^{(l)}$ and $B^{(l)}$.
  end for
  update record-specific parameters.
end while
for each query depth d **do**
  predict the age $A(d)$ in terms of the posterior samples $\left\{A^{(l)}(d)\right\}_{l=1}^L$ given $\left\{F_Z^{(l)}, B^{(l)}\right\}_{l=1}^L$ by Equation (A6).
end for

https://doi.org/10.5194/egusphere-2026-2299
Preprint. Discussion started: 24 June 2026

Appendix B: Training Dataset

Core	Lat °N	Lon °E	Depth m	References
A7	27.8	127.0	1264	Sun et al. (2005)
GeoB1711-4	-23.3	12.4	1967	Vidal et al. (1999); Balmer et al. (2016)
GeoB3302-1	-33.2	287.9	1498	Behling et al. (2015)
GeoB3304-5	-32.9	287.8	2411	Bernhardt et al. (2015)
GeoB3369-1	-30.4	288.0	3467	Bernhardt et al. (2015)
GeoB3606-1	-25.5	13.1	1785	Romero et al. (2003)
GeoB4905-4	2.5	9.4	1328	Weldeab et al. (2005); Adegbie et al. (2003)
GeoB6308-3	-39.3	306.0	3620	Voigt et al. (2015)
GeoB7920-2	20.8	341.4	2278	Collins et al. (2011)
GeoB7926-2	20.2	341.5	2500	McKay et al. (2014)
GeoB10053-7	-8.7	112.9	1372	Mohtadi et al. (2011)
GeoB10069-3	-9.6	120.9	1250	Gibbons et al. (2014)
GeoB13601-4	12.4	342.0	2997	Just et al. (2012)
GeoB13862-1	-38.0	306.3	3588	Voigt et al. (2015)
GeoB16202-2	-1.9	318.4	2248	Mulitza et al. (2017)
GeoB16206-1	-1.6	317.0	1367	Zhang et al. (2015)
GeoB16224-1	6.7	307.9	2510	Zhang et al. (2015)
GEOFARKF13	37.6	328.2	2690	Richter (2001)
GIK16160-3	-18.2	37.9	1339	Wang et al. (2013)
GIK17286-1	19.7	89.9	1428	Lauterbach et al. (2020)
GIK17748-2	-32.8	288.0	2545	Mohtadi (2010)
GIK17940-2	20.1	117.4	1727	Wang et al. (1999c)
GIK17961-2	8.5	112.3	1795	Wang et al. (1999a)
GIK17964-2	6.2	112.2	1556	Wang et al. (1999b)
GIK18519-2	-0.6	118.1	1658	Schröder et al. (2018)
GIK18526-3	-3.6	118.2	1524	Schröder et al. (2018)
GL-1090	-24.9	317.5	2225	Santos et al. (2017)
GL-1248	-0.9	316.6	2264	Venancio et al. (2018)
GL-74	-21.3	320.0	1279	Da Costa Portilho-Ramos et al. (2014)
HER-GC-ALB2	36.0	355.7	1313	Català et al. (2019)
IOW226660-5	-24.1	12.8	1821	Mollenhauer et al. (2003)
IOW226920-3	-22.5	12.4	1683	Mollenhauer et al. (2003)
KF13	37.6	328.2	2690	Richter (1998)
KNR140-39GGC	31.7	284.6	2975	Keigwin and Schlegel (2002)
KNR140-51GGC	32.8	283.7	1790	Keigwin (2004); Rasmussen and Thomsen (2012)
KNR159-5-22GGC	-29.8	316.4	3924	Hoffman and Lund (2012)
KNR159-5-36GGC	-27.3	313.5	1268	Came et al. (2003); Sortor and Lund (2011)
KNR197-10-17GGC	36.4	311.5	5010	Keigwin and Swift (2017)

https://doi.org/10.5194/egusphere-2026-2299
Preprint. Discussion started: 24 June 2026

KNR31-GPC5	33.7	302.4	4583	Keigwin et al. (1991); Keigwin and Jones (1994)
M35003-4	12.1	298.8	1299	Rühlemann et al. (1999); Mulitza et al. (2022); Hüls and Zahn (2000)
MD00-2361	-22.1	113.5	1805	Spooner et al. (2011)
MD01-2378	-13.1	121.8	1783	Holbourn et al. (2005)
MD01-2421	36.0	141.8	2224	Oba and Murayama (2004)
MD02-2550	26.9	268.7	2248	Williams et al. (2010); LoDico et al. (2006)
MD02-2594	-34.7	17.3	2440	Martínez-Méndez et al. (2010)
MD03-2611G	-36.7	136.5	2420	Gingele et al. (2007); Moros et al. (2009); De Deckker et al. (2012)
MD03-2698	38.2	349.6	4602	Lebreiro et al. (2009)
MD03-2707	2.5	9.4	1295	Weldeab et al. (2016, 2007)
MD05-2896	8.8	111.4	1657	Tian et al. (2010); Wan and Jian (2014)
MD05-2904	19.5	116.3	2066	Wan and Jian (2014)
MD05-2925	-9.3	151.5	1661	Lo et al. (2014)
MD06-3067	6.5	126.5	1575	Bolliet et al. (2011)
MD06-3075	6.5	125.8	1878	Fraser et al. (2014)
MD08-3180	38.0	328.9	3064	Schwab et al. (2012)
MD10-3340	-0.5	128.7	1094	Dang et al. (2020)
MD76-131	15.5	72.6	1230	Singh et al. (2011)
MD95-2043	36.1	357.4	1841	Cacho et al. (1999)
MD97-2138	1.3	146.1	1960	De Garidel-Thoron et al. (2007)
MD97-2151	8.7	109.9	1598	Lee et al. (1999)
MD98-2176	-5.0	133.4	2382	Stott et al. (2007)
MD98-2181	6.3	125.8	2114	Stott et al. (2007)
MD99-2334	37.8	349.8	3146	Skinner and Shackleton (2004, 2005); Skinner et al. (2003)
ME0005-24JC	0.0	273.5	2941	Kusch et al. (2010); Dubois et al. (2011)
ME0005A-43JC	7.9	276.4	1368	Benway et al. (2006)
MS21PC	32.3	31.6	1022	Hennekam et al. (2015)
ODP1145	19.6	117.6	3175	Oppo and Sun (2005)
ODP769	8.8	121.3	3656	Linsley (1996)
POS200_10_6-2	37.8	350.5	1086	Baas et al. (1997)
RC12-344	12.8	96.1	2140	Rashid et al. (2007)
SHAK06-5K	37.6	349.9	2646	Ausín et al. (2019)
SK237-GC04	11.0	75.0	1245	Saraswat et al. (2013)
SO42-74KL	14.3	57.3	3212	Sirocko et al. (1993)
SO50-31KL	18.8	115.9	3360	Chen and Huang (1998)
SU81-18	37.8	349.8	3155	Waelbroeck et al. (2019)
TGS-931	-2.4	122.6	1912	Schröder et al. (2018)
TR163-22	0.5	267.6	2830	Lea et al. (2006)
V19-30	-3.4	276.5	3091	Shackleton et al. (1983); Bond et al. (1997)
V35-5	7.2	112.1	1953	Broecker et al. (1988); Andree et al. (1986)
VM12-107	11.3	293.4	1079	Schmidt et al. (2012)

https://doi.org/10.5194/egusphere-2026-2299
Preprint. Discussion started: 24 June 2026

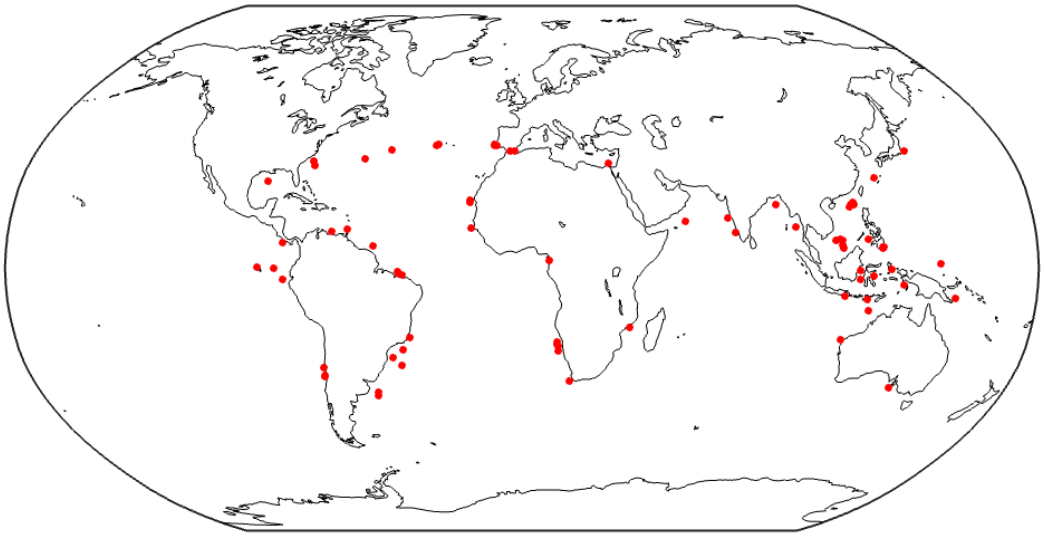

Figure B1. Locations of 79 records.

https://doi.org/10.5194/egusphere-2026-2299
Preprint. Discussion started: 24 June 2026

Appendix C: Supplementary Figures and Tables

α	0.05	0.1	0.2	0.5	1.0	2.0
0.5	0.497	0.497	0.497	0.498	0.497	0.494
1.0	0.988	0.988	0.988	0.988	0.988	0.981
1.5	1.460	1.460	1.461	1.461	1.460	1.450
2.0	1.922	1.922	1.922	1.922	1.923	1.921
2.5	2.389	2.389	2.389	2.390	2.391	2.394
3.0	2.858	2.858	2.858	2.859	2.862	2.867

Table C1. The estimated β in Section 5.1. Each column corresponds to the interval length of standardized $Z^{(p)}$.

α	0.05	0.1	0.2	0.5	1.0	2.0
0.5	0.021	0.020	0.014	0.002	0.001	0.260
1.0	0.249	0.248	0.245	0.229	0.239	0.363
1.5	0.524	0.519	0.519	0.518	0.525	0.581
2.0	0.635	0.634	0.634	0.635	0.630	0.633
2.5	0.674	0.674	0.674	0.671	0.666	0.657
3.0	0.698	0.697	0.697	0.695	0.689	0.676

Table C2. The estimated ρ in Section 5.1. Each column corresponds to the interval length of standardized $Z^{(p)}$.

α	0.05	0.1	0.2	0.5	1.0	2.0
0.5	0.563	0.558	0.558	0.610	0.847	1.338
1.0	1.151	1.153	1.151	1.169	1.285	1.650
1.5	1.698	1.693	1.691	1.703	1.751	1.950
2.0	2.041	2.038	2.042	2.044	2.052	2.149
2.5	2.259	2.258	2.254	2.259	2.252	2.306
3.0	2.456	2.455	2.458	2.449	2.438	2.467

Table C3. The empirical $\tilde{\alpha}$ in Section 5.1. Each column corresponds to the interval length of standardized $Z^{(p)}$.

https://doi.org/10.5194/egusphere-2026-2299
Preprint. Discussion started: 24 June 2026

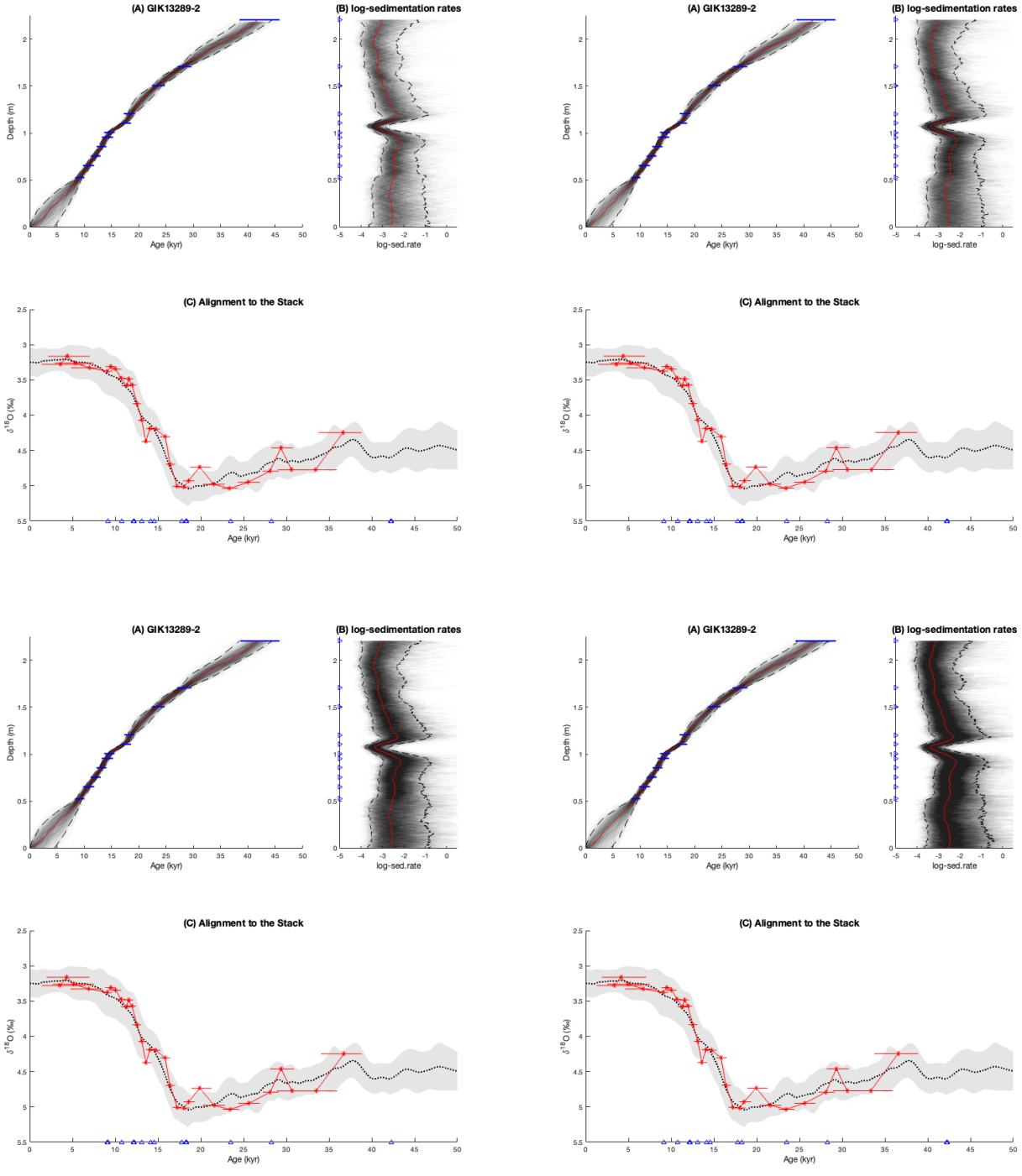

Figure C1. Age estimation results of GIK13289-2 for the standardized interval lengths of 0.9483, 0.4808, 0.2395 and 0.1196.

https://doi.org/10.5194/egusphere-2026-2299
Preprint. Discussion started: 24 June 2026

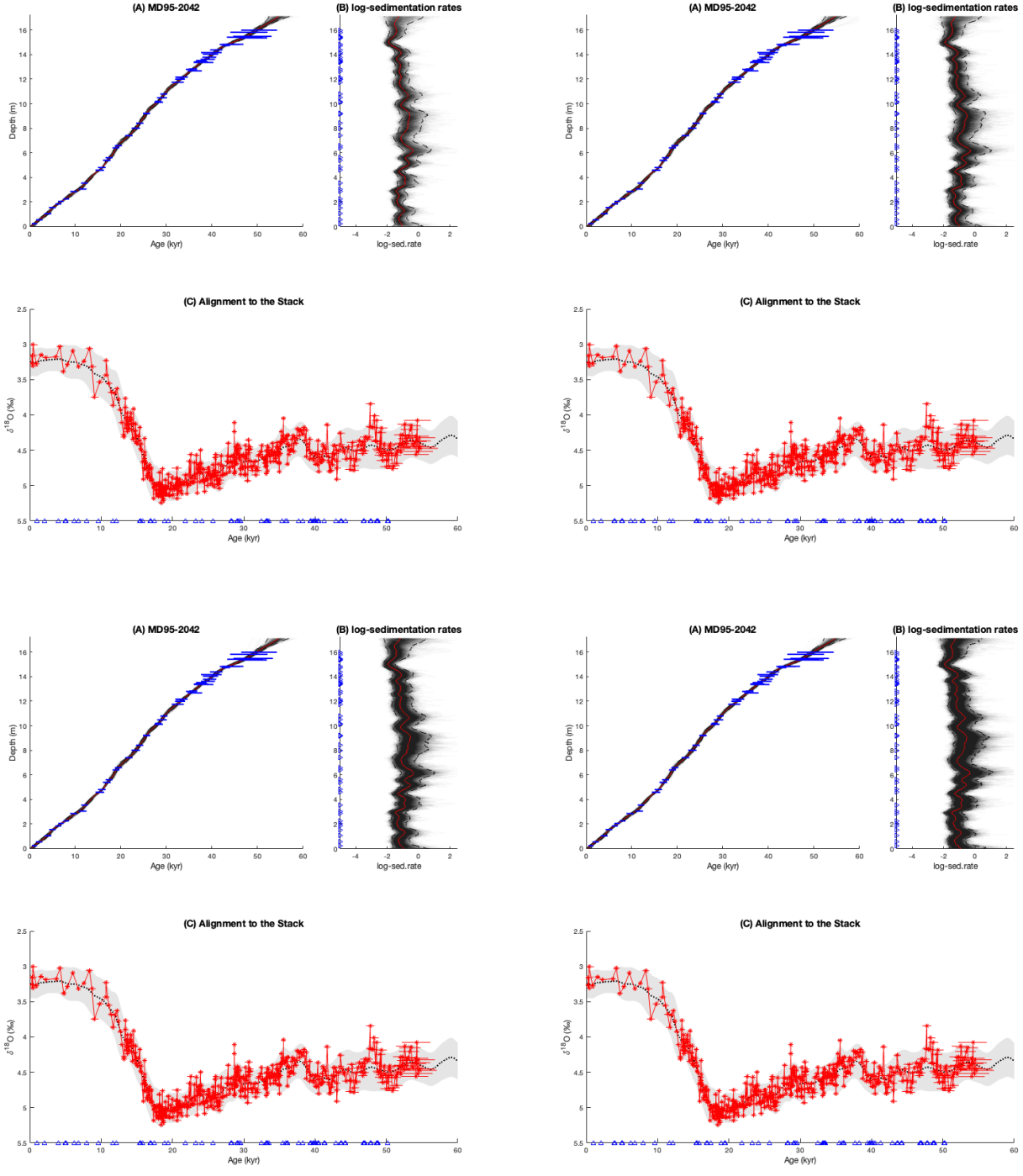

Figure C2. Age estimation results of MD95-2042 (up to 17.2 meters) for the standardized interval lengths of 1.0297, 0.5129, 0.2565 and 0.1285.

https://doi.org/10.5194/egusphere-2026-2299
Preprint. Discussion started: 24 June 2026

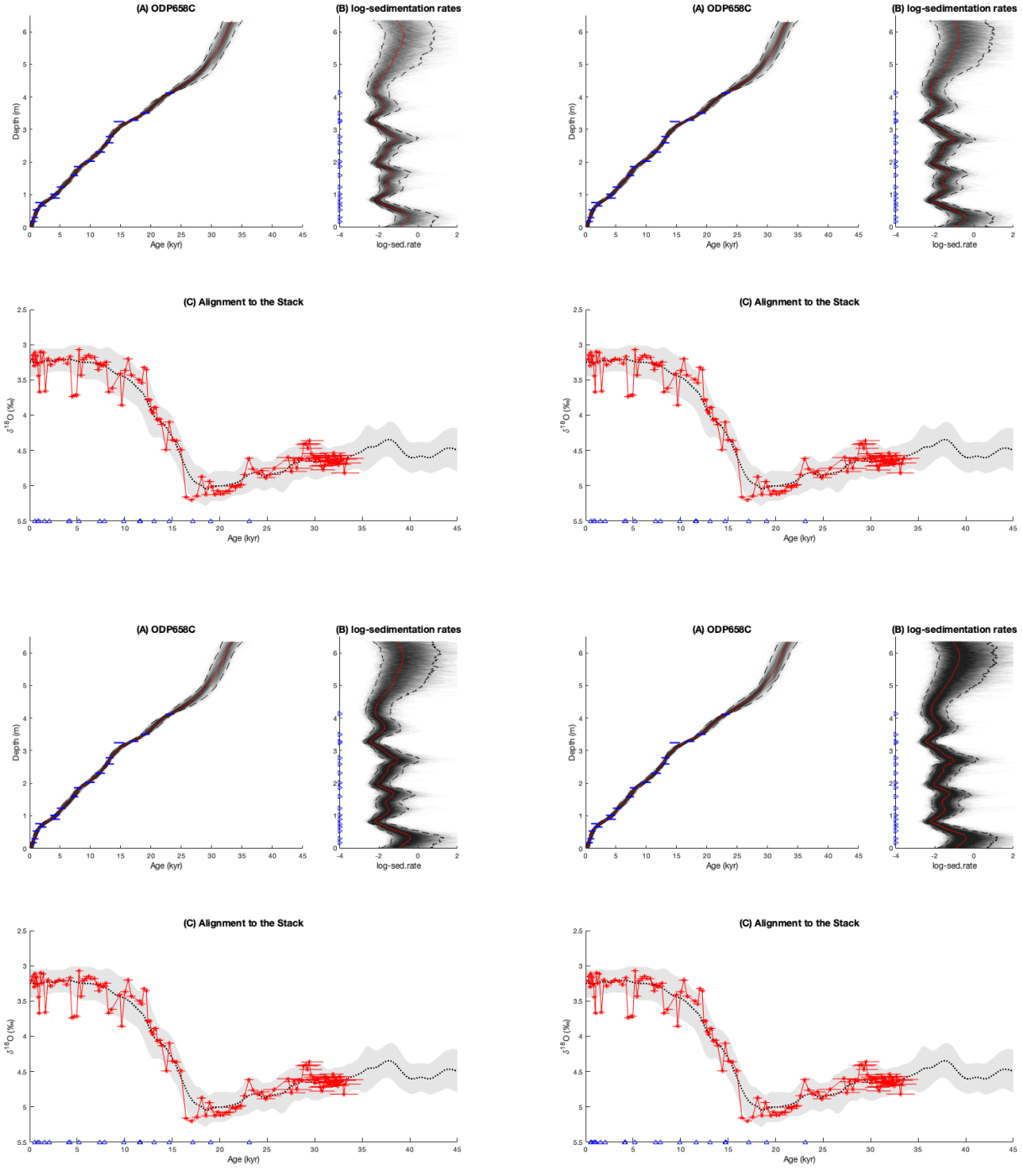

Figure C3. Age estimation results of ODP658C for the standardized interval lengths of 0.9237, 0.4606, 0.2309 and 0.1153.

https://doi.org/10.5194/egusphere-2026-2299
Preprint. Discussion started: 24 June 2026

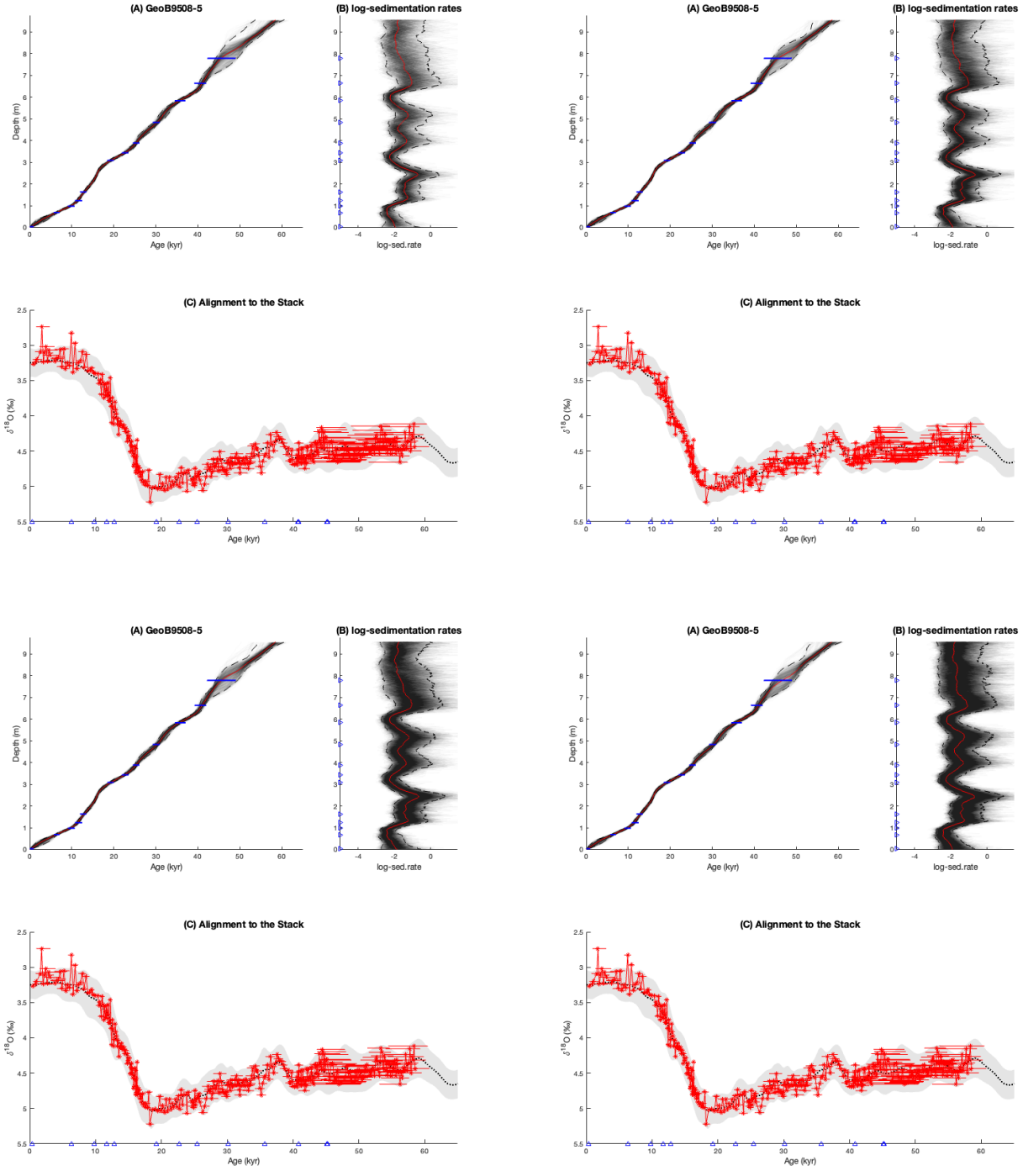

Figure C4. Age estimation results of GeoB9508-5 for the standardized interval lengths of 1.0365, 0.5193, 0.2610 and 0.1301.

https://doi.org/10.5194/egusphere-2026-2299
Preprint. Discussion started: 24 June 2026

Code and data availability. The codes and data that support the findings of this study are openly available with an instruction manual, downloaded from https://doi.org/10.5281/zenodo.19701785 (Lee, 2026b). In particular, Algorithm A2 is also implemented in Python, which can be downloaded from https://doi.org/10.5281/zenodo.19700415 (Lee, 2026a).

Author contributions. Taehee Lee contributed to conceptualization, formal analysis, funding acquisition, methodology, software, validation, visualization, writing (original draft); Lorraine E. Lisiecki contributed to conceptualization, funding acquisition, writing (original draft); Samuel Newall contributed to conceptualization, data curation, visualization, writing (original draft); Yuxin Zhou contributed to conceptualization, writing (original draft); and Charles E. Lawrence contributed to conceptualization, funding acquisition, writing (review & editing).

Competing interests. The contact author has declared that none of the authors has any competing interests.

Acknowledgements. This work is partially supported by NSF-OCE grant 2410906 awarded to Taehee Lee and Charles E. Lawrence; NSF-OCE grant 2508421 awarded to Lorraine E. Lisiecki and Samuel Newall; and NSF-OCE 2508422 awarded to Charles E. Lawrence and Taehee Lee.

https://doi.org/10.5194/egusphere-2026-2299
Preprint. Discussion started: 24 June 2026

References

Adegbie, A. T., Schneider, R. R., Röhl, U., and Wefer, G.: (Table 1) Radiocarbon (14C) ages of sediment core GeoB4905-4, https://doi.org/10.1594/PANGAEA.117007, 2003.

Ahn, S., Khider, D., Lisiecki, L. E., and Lawrence, C. E.: A probabilistic Pliocene–Pleistocene stack of benthic δ18O using a profile hidden Markov model, Dynamics and Statistics of the Climate System, 2, dzx002, https://doi.org/10.1093/climsys/dzx002, 2017.

Andree, M., Oeschger, H., Broecker, W., Beavan, N., Klas, M., Mix, A., Bonani, G., Hofmann, H. J., Suter, M., Woelfli, W., and Peng, T.-H.: Limits on the ventilation rate for the deep ocean over the last 12000 years, Climate Dynamics, 1, 53–62, https://doi.org/10.1007/BF01277046, 1986.

Ausín, B., Haghipour, N., Wacker, L., Voelker, A. H. L., Hodell, D. A., Magill, C., Looser, N., Bernasconi, S. M., and Eglinton, T. I.: Radiocarbon and calendar ages of monospecific samples of the planktonic foraminifera Globigerina bulloides from sediment core SHAK06-5K, https://doi.org/10.1594/PANGAEA.898607, 2019.

Baas, J., Mienert, J., Abrantes, F., and Prins, M.: Late Quaternary sedimentation on the Portuguese continental margin: climate-related processes and products, Palaeogeography, Palaeoclimatology, Palaeoecology, 130, 1–23, https://doi.org/10.1016/S0031-0182(96)00135-6, 1997.

Balmer, S., Sarnthein, M., Mudelsee, M., and Grootes, P. M.: (Table S3a) 14C ages measured on Globigerina bulloides of sediment core GeoB1711-4, https://doi.org/10.1594/PANGAEA.863647, 2016.

Banerjee, S., Carlin, B., and Gelfand, A.: Hierarchical Modeling and Analysis for Spatial Data (2nd ed.), Chapman and Hall/CRC, https://doi.org/https://doi.org/10.1201/b17115, 2014.

Bard, E., Fairbanks, R., Arnold, M., Maurice, P., Duprat, J., Moyes, J., and Duplessy, J.-C.: Sea-level estimates during the last deglaciation based on d18O and accelerator mass spectrometry 14C ages measured in Globigerina bulloides, Quaternary Research, 31, 381–391, https://doi.org/https://doi.org/10.1016/0033-5894(89)90045-8, 1989.

Bard, E., Rostek, F., and Ménot-Combes, G.: Radiocarbon calibration beyond 20,000 14C yr B.P. by means of planktonic foraminifera of the Iberian Margin, Quaternary Research, 61, 204–214, https://doi.org/https://doi.org/10.1016/j.yqres.2003.11.006, 2004.

Bard, E., Ménot, G., Rostek, F., Licari, L., Böning, P., Edwards, R. L., Cheng, H., Wang, Y., and Heaton, T. J.: Radiocarbon Calibration/Comparison Records Based on Marine Sediments from the Pakistan and Iberian Margins, Radiocarbon, 55, 1999–2019, https://doi.org/10.2458/azu_js_rc.55.17114, 2013.

Barndorff-Nielsen, O. E. and Shephard, N.: Integrated OU Processes and Non-Gaussian OU-Based Stochastic Volatility Models, Scandinavian Journal of Statistics, 30, 277–295, http://www.jstor.org/stable/4616764, 2003.

Bassis, J. N., Petersen, S. V., and Mac Cathles, L.: Heinrich events triggered by ocean forcing and modulated by isostatic adjustment, Nature, 542, 332—334, https://doi.org/10.1038/nature21069, 2017.

Behling, H., Arz, H. W., Pätzold, J., and Wefer, G.: (Table 1) List of reservoir-corrected (~420 yr) AMS radiocarbon dates of sediment core GeoB3202-1, https://doi.org/10.1594/PANGAEA.851377, 2015.

Benway, H. M., Mix, A. C., Haley, B. A., and Klinkhammer, G. P.: (Table S1) Age determination of sediment core ME0005A-43JC, https://doi.org/10.1594/PANGAEA.834477, 2006.

Bernhardt, A., Melnick, D., Hebbeln, D., Lückge, A., and Strecker, M. R.: (Appendix A) Radiocarbon ages of sediment cores along the continental margin of Chile, https://doi.org/10.1594/PANGAEA.853962, 2015.

https://doi.org/10.5194/egusphere-2026-2299
Preprint. Discussion started: 24 June 2026

Blaauw, M. and Christen, J. A.: Flexible paleoclimate age-depth models using an autoregressive gamma process, Bayesian Analysis, 6, 457 – 474, https://doi.org/10.1214/11-BA618, 2011.

Bolliet, T., Holbourn, A. E., Kuhnt, W., Kissel, C., Beaufort, L., Kienast, M., Andersen, N., and Garbe-Schönberg, D.: Age determination of sediment core MD06-3067, https://doi.org/10.1594/PANGAEA.770287, 2011.

Bond, G., Showers, W., Cheseby, M., Lotti, R., Almasi, P., deMenocal, P., Priore, P., Cullen, H., Hajdas, I., and Bonani, G.: A Pervasive Millennial-Scale Cycle in North Atlantic Holocene and Glacial Climates, Science, 278, 1257–1266, https://doi.org/10.1126/science.278.5341.1257, 1997.

Broecker, W. S., Andree, M., Klas, M., Bonani, G., Wolfli, W., and Oeschger, H.: New evidence from the South China Sea for an abrupt termination of the last glacial period, Nature, 333, 156–158, https://doi.org/10.1038/333156a0, 1988.

Brooks, S., Gelman, A., Jones, G., and Meng, X.-L.: Handbook of Markov Chain Monte Carlo (1st ed.), Chapman and Hall/CRC, 2011.

Cacho, I., Grimalt, J. O., Pelejero, C., Canals, M., Sierro, F. J., Flores, J.-A., and Shackleton, N. J.: (Table 1) Age determination of sediment core MD95-2043, https://doi.org/10.1594/PANGAEA.735758, 1999.

Came, R. E., Oppo, D. W., and Curry, W. B.: Atlantic Ocean circulation during the Younger Dryas: Insights from a new Cd/Ca record from the western subtropical South Atlantic, Paleoceanography, 18, 2003PA000 888, https://doi.org/10.1029/2003PA000888, 2003.

Català, A., Cacho, I., Frigola, J., Pena, L. D., and Lirer, F.: Age-model update from sediment core HER-GC-ALB2 (ALB-2), https://doi.org/10.1594/PANGAEA.901744, 2019.

Channell, J., Singer, B., and Jicha, B.: Timing of Quaternary geomagnetic reversals and excursions in volcanic and sedimentary archives, Quaternary Science Reviews, 228, 106 114, https://doi.org/https://doi.org/10.1016/j.quascirev.2019.106114, 2020.

Chen, M. and Huang, C.: Ice-volume forcing of winter monsoon climate in the South China Sea, Paleoceanography, 13, 622–633, https://doi.org/10.1029/98PA02356, 1998.

Christen, J. A. and Pérez E, S.: A New Robust Statistical Model for Radiocarbon Data, Radiocarbon, 51, 1047–1059, https://doi.org/10.1017/S003382220003410X, 2009.

Collins, J. A., Schefuß, E., Heslop, D., Prange, M., Zabel, M., Tjallingii, R., Dokken, T., Huang, E., Mackensen, A., Schulz, M., Tian, J., Zarriess, M., and Wefer, G.: Age models of sediment cores GeoB7920-2 and GeoB9535-4, https://doi.org/10.1594/PANGAEA.757419, 2011.

Cooper, A., Turney, C. S. M., Palmer, J., Hogg, A., McGlone, M., Wilmshurst, J., Lorrey, A. M., Heaton, T. J., Russell, J. M., McCracken, K., Anet, J. G., Rozanov, E., Friedel, M., Suter, I., Peter, T., Muscheler, R., Adolphi, F., Dosseto, A., Faith, J. T., Fenwick, P., Fogwill, C. J., Hughen, K., Lipson, M., Liu, J., Nowaczyk, N., Rainsley, E., Ramsey, C. B., Sebastianelli, P., Souilmi, Y., Stevenson, J., Thomas, Z., Tobler, R., and Zech, R.: A global environmental crisis 42,000 years ago, Science, 371, 811–818, https://doi.org/10.1126/science.abb8677, 2021.

Cox, J. C., Ingersoll, J. E., and Ross, S. A.: A Theory of the Term Structure of Interest Rates, Econometrica, 53, 385–407, http://www.jstor.org/stable/1911242, 1985.

Da Costa Portilho-Ramos, R., Ferreira, F., Lago, L. C., Da Silva, A. G. V., Jaworski, K. S., and De Toledo, M. B.: GLOBOROTALIA CRASSAFORMIS OPTIMUM EVENT: A NEW LATE QUATERNARY BIOSTRATIGRAPHIC MARKER FOR THE SOUTHEASTERN BRAZILIAN MARGIN, PALAIOS, 29, 578–593, https://doi.org/10.2110/palo.2013.097, 2014.

Dang, H., Jian, Z., Kissel, C., and Bassinot, F.: Age and sediment geochemical data of MD10-3340, Halmahera Sea, https://doi.org/10.1594/PANGAEA.924044, medium: application/zip, 2020.

De Deckker, P., Moros, M., Perner, K., and Jansen, E.: Influence of the tropics and southern westerlies on glacial interhemispheric asymmetry, Nature Geoscience, 5, 266–269, https://doi.org/10.1038/ngeo1431, 2012.

https://doi.org/10.5194/egusphere-2026-2299
Preprint. Discussion started: 24 June 2026

De Garidel-Thoron, T., Rosenthal, Y., Beaufort, L., Bard, E., Sonzogni, C., and Mix, A. C.: A multiproxy assessment of the western equatorial Pacific hydrography during the last 30 kyr, Paleoceanography, 22, 2006PA001 269, https://doi.org/10.1029/2006PA001269, 2007.

deMenocal, P., Ortiz, J., Guilderson, T., Adkins, J., Sarnthein, M., Baker, L., and Yarusinsky, M.: Abrupt onset and termination of the African Humid Period:: rapid climate responses to gradual insolation forcing, Quaternary Science Reviews, 19, 347–361, https://doi.org/https://doi.org/10.1016/S0277-3791(99)00081-5, 2000.

Dempster, A. P., Laird, N. M., and Rubin, D. B.: Maximum likelihood from incomplete data via the EM algorithm, JOURNAL OF THE ROYAL STATISTICAL SOCIETY, SERIES B, 39, 1–38, 1977.

Doughty, A. M., Kaplan, M. R., Peltier, C., and Barker, S.: A maximum in global glacier extent during MIS 4, Quaternary Science Reviews, 261, 106 948, https://doi.org/https://doi.org/10.1016/j.quascirev.2021.106948, 2021.

Dubois, N., Kienast, M., Kienast, S., Normandeau, C., Calvert, S. E., Herbert, T. D., and Mix, A.: Millennial-scale variations in hydrography and biogeochemistry in the Eastern Equatorial Pacific over the last 100 kyr, Quaternary Science Reviews, 30, 210–223, https://doi.org/10.1016/j.quascirev.2010.10.012, 2011.

Fraser, N., Kuhnt, W., Holbourn, A. E., Bolliet, T., Andersen, N., Blanz, T., and Beaufort, L.: Age model of sediment core MD06-3075, https://doi.org/10.1594/PANGAEA.837180, 2014.

Gelman, A., Carlin, J., Stern, H., Dunson, D., Vehtari, A., and Rubin, D.: Bayesian Data Analysis, Chapman & Hall/CRC Texts in Statistical Science, CRC Press, ISBN 9781439898208, https://books.google.com/books?id=eSHSBQAAQBAJ, 2013.

Gibbons, F. T., Oppo, D. W., Mohtadi, M., Rosenthal, Y., Cheng, J., Liu, Z., and Linsley, B. K.: Deglacial δ18O and hydrologic variability in the tropical Pacific and Indian Oceans, Earth and Planetary Science Letters, 387, 240–251, https://doi.org/10.1016/j.epsl.2013.11.032, 2014.

Gingele, F., De Deckker, P., and Norman, M.: Late Pleistocene and Holocene climate of SE Australia reconstructed from dust and river loads deposited offshore the River Murray Mouth, Earth and Planetary Science Letters, 255, 257–272, https://doi.org/10.1016/j.epsl.2006.12.019, 2007.

Golub, G. H. and Van Loan, C. F.: Matrix Computations - 4th Edition, Johns Hopkins University Press, Philadelphia, PA, https://doi.org/10.1137/1.9781421407944, 2013.

Haslett, J. and Parnell, A.: A Simple Monotone Process with Application to Radiocarbon-Dated Depth Chronologies, Journal of the Royal Statistical Society Series C: Applied Statistics, 57, 399–418, https://doi.org/10.1111/j.1467-9876.2008.00623.x, 2008.

Hawks, J.: Comment on "A global environmental crisis 42,000 years ago", Science, 374, eabh1878, https://doi.org/10.1126/science.abh1878, 2021.

Heaton, T. J., Köhler, P., Butzin, M., Bard, E., Reimer, R. W., Austin, W. E. N., Bronk Ramsey, C., Grootes, P. M., Hughen, K. A., Kromer, B., and et al.: Marine20—The Marine Radiocarbon Age Calibration Curve (0–55,000 cal BP), Radiocarbon, 62, 779–820, https://doi.org/10.1017/RDC.2020.68, 2020.

Hemming, S. R.: Heinrich events: Massive late Pleistocene detritus layers of the North Atlantic and their global climate imprint, Reviews of Geophysics, 42, https://doi.org/https://doi.org/10.1029/2003RG000128, 2004.

Hennekam, R., Donders, T. H., Zwiep, K., and De Lange, G. J.: Integral view of Holocene precipitation and vegetation changes in the Nile catchment area as inferred from its delta sediments, Quaternary Science Reviews, 130, 189–199, https://doi.org/10.1016/j.quascirev.2015.05.031, 2015.

Hoffman, J. L. and Lund, D. C.: Refining the stable isotope budget for Antarctic Bottom Water: New foraminiferal data from the abyssal southwest Atlantic, Paleoceanography, 27, 2011PA002 216, https://doi.org/10.1029/2011PA002216, 2012.

https://doi.org/10.5194/egusphere-2026-2299
Preprint. Discussion started: 24 June 2026

Holbourn, A. E., Kuhnt, W., Kawamura, H., Jian, Z., Grootes, P. M., Erlenkeuser, H., and Xu, J.: (Table 2) Age determination of sediment core MD01-2378, https://doi.org/10.1594/PANGAEA.738104, 2005.

Hüls, M. and Zahn, R.: Millennial-scale sea surface temperature variability in the western tropical North Atlantic from planktonic foraminiferal census counts, Paleoceanography, 15, 659–678, https://doi.org/10.1029/1999PA000462, 2000.

Jeanblanc, M., Yor, M., and M., C.: Mathematical Methods for Financial Markets, Springer London, ISBN 978-1-85233-376-8, 2009.

Just, J., Dekkers, M. J., Von Dobeneck, T., Van Hoesel, A., and Bickert, T.: Signatures and significance of aeolian, fluvial, bacterial and diagenetic magnetic mineral fractions in Late Quaternary marine sediments off Gambia, NW Africa, Geochemistry, Geophysics, Geosystems, 13, 2012GC004 146, https://doi.org/10.1029/2012GC004146, 2012.

Keigwin, L. D.: Radiocarbon and stable isotope constraints on Last Glacial Maximum and Younger Dryas ventilation in the western North Atlantic, Paleoceanography, 19, 2004PA001 029, https://doi.org/10.1029/2004PA001029, 2004.

Keigwin, L. D. and Jones, G. A.: Western North Atlantic evidence for millennial-scale changes in ocean circulation and climate, Journal of Geophysical Research: Oceans, 99, 12 397–12 410, https://doi.org/10.1029/94JC00525, 1994.

Keigwin, L. D. and Schlegel, M. A.: Ocean ventilation and sedimentation since the glacial maximum at 3 km in the western North Atlantic, Geochemistry, Geophysics, Geosystems, 3, 1–14, https://doi.org/10.1029/2001GC000283, 2002.

Keigwin, L. D. and Swift, S. A.: Carbon isotope evidence for a northern source of deep water in the glacial western North Atlantic, Proceedings of the National Academy of Sciences, 114, 2831–2835, https://doi.org/10.1073/pnas.1614693114, 2017.

Keigwin, L. D., Jones, G. A., Lehman, S. J., and Boyle, E. A.: Deglacial meltwater discharge, North Atlantic Deep Circulation, and abrupt climate change, Journal of Geophysical Research: Oceans, 96, 16 811–16 826, https://doi.org/10.1029/91JC01624, 1991.

Knaack, J.-J. and Sarnthein, M.: Stable isotopes of foraminifera of ODP Hole 108-658C, https://doi.org/10.1594/PANGAEA.227736, 2005.

Kusch, S., Eglinton, T. I., Mix, A. C., and Mollenhauer, G.: Timescales of lateral sediment transport in the Panama Basin as revealed by radiocarbon ages of alkenones, total organic carbon and foraminifera, Earth and Planetary Science Letters, 290, 340–350, https://doi.org/10.1016/j.epsl.2009.12.030, 2010.

Lauterbach, S., Andersen, N., Wang, Y. V., Blanz, T., Larsen, T., and Schneider, R. R.: An ~130 kyr Record of Surface Water Temperature and δ^{18} O From the Northern Bay of Bengal: Investigating the Linkage Between Heinrich Events and Weak Monsoon Intervals in Asia, Paleoceanography and Paleoclimatology, 35, e2019PA003 646, https://doi.org/10.1029/2019PA003646, 2020.

Lea, D. W., Pak, D. K., Belanger, C. L., Spero, H. J., Hall, M. A., and Shackleton, N. J.: Paleoclimate history of Galápagos surface waters over the last 135,000yr, Quaternary Science Reviews, 25, 1152–1167, https://doi.org/10.1016/j.quascirev.2005.11.010, 2006.

Lebreiro, S. M., Voelker, A. H. L., Vizcaino, A., Abrantes, F. F., Alt-Epping, U., Jung, S., Thouveny, N., and Gràcia, E.: (Table 1) AMS 14C measurements in sediment core MD03-2698, https://doi.org/10.1594/PANGAEA.733491, 2009.

Lee, M.-Y., Wei, K.-Y., and Chen, Y.-G.: High Resolution Oxygen Isotope Straigraphy for the Last 150,000 Years in the Southern South China Sea:Core MD972151, Terrestrial, Atmospheric and Oceanic Sciences, 10, 239, https://doi.org/10.3319/TAO.1999.10.1.239(IMAGES), 1999.

Lee, T.: CIR Process Age Inference Algorithm for Age Estimation (Python), https://doi.org/10.5281/zenodo.19700415, 2026a.

Lee, T.: CIR Process Age Inference Algorithm for Age Estimation (MATLAB), https://doi.org/10.5281/zenodo.19701785, 2026b.

Lee, T., Rand, D., Lisiecki, L. E., Gebbie, G., and Lawrence, C.: Bayesian age models and stacks: combining age inferences from radiocarbon and benthic δ^{18}O stratigraphic alignment, Climate of the Past, 19, 1993–2012, https://doi.org/10.5194/cp-19-1993-2023, 2023.

Lin, L., Khider, D., Lisiecki, L. E., and Lawrence, C. E.: Probabilistic sequence alignment of stratigraphic records, Paleoceanography, 29, 976–989, https://doi.org/https://doi.org/10.1002/2014PA002713, 2014.

https://doi.org/10.5194/egusphere-2026-2299
Preprint. Discussion started: 24 June 2026

Linsley, B. K.: Oxygen-isotope record of sea level and climate variations in the Sulu Sea over the past 150,000 years, Nature, 380, 234–237, https://doi.org/10.1038/380234a0, 1996.

Lisiecki, L. E. and Raymo, M. E.: A Pliocene-Pleistocene stack of 57 globally distributed benthic δ18O records, Paleoceanography, 20, https://doi.org/https://doi.org/10.1029/2004PA001071, 2005.

Lisiecki, L. E., Jones, A. M., Rand, D., Lee, T., and Lawrence, C. E.: Comparing age model techniques for the last glacial cycle: A case study of ten Iberian Margin sediment cores, Quaternary Science Reviews, 287, 107 559, https://doi.org/10.1016/j.quascirev.2022.107559, 2022.

Liu, J.: Monte Carlo Strategies in Scientific Computing, Springer New York, NY, https://doi.org/https://doi.org/10.1007/978-0-387-76371-2, 2004.

Liu, Q. and Wang, D.: Stein Variational Gradient Descent: A General Purpose Bayesian Inference Algorithm, in: Advances in Neural Information Processing Systems, edited by Lee, D., Sugiyama, M., Luxburg, U., Guyon, I., and Garnett, R., vol. 29, Curran Associates, Inc., https://proceedings.neurips.cc/paper_files/paper/2016/file/b3ba8f1bee1238a2f37603d90b58898d-Paper.pdf, 2016.

Lo, L., Shen, C.-C., Wei, K.-Y., Burr, G. S., Mii, H.-S., Chen, M.-T., Lee, S.-Y., and Tsai, M.-C.: Millennial meridional dynamics of the Indo-Pacific Warm Pool during the last termination, Climate of the Past, 10, 2253–2261, https://doi.org/10.5194/cp-10-2253-2014, 2014.

LoDico, J. M., Flower, B. P., and Quinn, T. M.: Subcentennial-scale climatic and hydrologic variability in the Gulf of Mexico during the early Holocene, Paleoceanography, 21, 2005PA001 243, https://doi.org/10.1029/2005PA001243, 2006.

L'Ecuyer, P., Munger, D., and Tuffin, B.: On the distribution of integration error by randomly-shifted lattice rules, Electronic Journal of Statistics, 4, 950 – 993, https://doi.org/10.1214/10-EJS574, 2010.

Martínez-Méndez, G., Zahn, R., Hall, I. R., Peeters, F. J. C., Pena, L. D., Cacho, I., and Negre, C.: (Table S1) Globorotalia inflata 14C AMS ages and calibrated calendar year ages for core MD02-2594, https://doi.org/10.1594/PANGAEA.810668, 2010.

McCarthy, A., Mackintosh, A., Rieser, U., and Fink, D.: Mountain Glacier Chronology from Boulder Lake, New Zealand, Indicates MIS 4 and MIS 2 Ice Advances of Similar Extent, Arctic, Antarctic, and Alpine Research, 40, 695–708, https://doi.org/10.1657/1523-0430(06-111)[MCCARTHY]2.0.CO;2, 2008.

McKay, C. L., Filipsson, H. L., Romero, O. E., Stuut, J.-B. W., and Donner, B.: (Table 1) AMS 14C dates and calibrated calendar dates of sediment core GeoB7926-2, https://doi.org/10.1594/PANGAEA.847823, 2014.

Mishura, Y., Pilipenko, A., and Yurchenko-Tytarenko, A.: Low-dimensional Cox-Ingersoll-Ross process, Stochastics, 96, 1530–1550, https://doi.org/10.1080/17442508.2023.2300291, 2024.

Mohtadi, M.: (Table 1) Radiocarbon age data of sediment core GIK17748-2, https://doi.org/10.1594/PANGAEA.733250, 2010.

Mohtadi, M., Oppo, D. W., Steinke, S., Stuut, J.-B. W., De Pol-Holz, R., Hebbeln, D., and Lückge, A.: (Table S1) Age control points of core GeoB10053-7, https://doi.org/10.1594/PANGAEA.767355, 2011.

Mollenhauer, G., Eglinton, T., Ohkouchi, N., Schneider, R., Müller, P., Grootes, P., and Rullkötter, J.: Asynchronous alkenone and foraminifera records from the Benguela Upwelling System, Geochimica et Cosmochimica Acta, 67, 2157–2171, https://doi.org/10.1016/S0016-7037(03)00168-6, 2003.

Moros, M., De Deckker, P., Jansen, E., Perner, K., and Telford, R. J.: Holocene climate variability in the Southern Ocean recorded in a deep-sea sediment core off South Australia, Quaternary Science Reviews, 28, 1932–1940, https://doi.org/10.1016/j.quascirev.2009.04.007, 2009.

Mulitza, S., Prange, M., Stuut, J.-B., Zabel, M., von Dobeneck, T., Itambi, A. C., Nizou, J., Schulz, M., and Wefer, G.: Sahel megadroughts triggered by glacial slowdowns of Atlantic meridional overturning, Paleoceanography, 23, https://doi.org/https://doi.org/10.1029/2008PA001637, 2008.

https://doi.org/10.5194/egusphere-2026-2299
Preprint. Discussion started: 24 June 2026

Mulitza, S., Chiessi, C. M., Schefuß, E., Lippold, J., Wichmann, D., Antz, B., Mackensen, A., Paul, A., Prange, M., Rehfeld, K., Werner, M., Bickert, T., Frank, N., Kuhnert, H., Lynch-Stieglitz, J., Portilho-Ramos, R. C., Sawakuchi, A. O., Schulz, M., Schwenk, T., Tiedemann, R., Vahlenkamp, M., and Zhang, Y.: Synchronous and proportional deglacial changes in Atlantic meridional overturning and northeast Brazilian precipitation, Paleoceanography, 32, 622–633, https://doi.org/10.1002/2017PA003084, 2017.

Mulitza, S., Bickert, T., Bostock, H. C., Chiessi, C. M., Donner, B., Govin, A., Harada, N., Huang, E., Johnstone, H., Kuhnert, H., Langner, M., Lamy, F., Lembke-Jene, L., Lisiecki, L., Lynch-Stieglitz, J., Max, L., Mohtadi, M., Mollenhauer, G., Muglia, J., Nürnberg, D., Paul, A., Rühlemann, C., Repschläger, J., Saraswat, R., Schmittner, A., Sikes, E. L., Spielhagen, R. F., and Tiedemann, R.: World Atlas of late Quaternary Foraminiferal Oxygen and Carbon Isotope Ratios, Earth System Science Data, 14, 2553–2611, https://doi.org/10.5194/essd-14-2553-2022, 2022.

Murphy, K. P.: Probabilistic Machine Learning: An introduction, MIT Press, http://probml.github.io/book1, 2022.

Murphy, K. P.: Probabilistic Machine Learning: Advanced Topics, MIT Press, http://probml.github.io/book2, 2023.

Oba, T. and Murayama, M.: Sea-surface temperature and salinity changes in the northwest Pacific since the Last Glacial Maximum, Journal of Quaternary Science, 19, 335–346, https://doi.org/10.1002/jqs.843, 2004.

Oppo, D. W. and Sun, Y.: Amplitude and timing of sea-surface temperature change in the northern South China Sea: Dynamic link to the East Asian monsoon, Geology, 33, 785, https://doi.org/10.1130/G21867.1, 2005.

Picin, A., Benazzi, S., Blasco, R., Hajdinjak, M., Helgen, K. M., Hublin, J.-J., Rosell, J., Skoglund, P., Stringer, C., and Talamo, S.: Comment on “A global environmental crisis 42,000 years ago”, Science, 374, eabi8330, https://doi.org/10.1126/science.abi8330, 2021.

Qu, Y., Dassios, A., and Zhao, H.: Exact simulation of gamma-driven Ornstein–Uhlenbeck processes with finite and infinite activity jumps, Journal of the Operational Research Society, 72, 471–484, https://doi.org/10.1080/01605682.2019.1657368, 2021.

Rashid, H., Hesse, R., and Piper, D. J. W.: Evidence for an additional Heinrich event between H5 and H6 in the Labrador Sea, Paleoceanography, 18, https://doi.org/https://doi.org/10.1029/2003PA000913, 2003.

Rashid, H., Flower, B., Poore, R., and Quinn, T.: A ~25ka Indian Ocean monsoon variability record from the Andaman Sea, Quaternary Science Reviews, 26, 2586–2597, https://doi.org/10.1016/j.quascirev.2007.07.002, 2007.

Rasmussen, C. E. and Williams, C. K. I.: Gaussian Processes for Machine Learning (Adaptive Computation and Machine Learning), The MIT Press, ISBN 026218253X, 2006.

Rasmussen, T. and Thomsen, E.: Changes in planktic foraminiferal faunas, temperature and salinity in the Gulf Stream during the last 30,000 years: influence of meltwater via the Mississippi River, Quaternary Science Reviews, 33, 42–54, https://doi.org/10.1016/j.quascirev.2011.11.019, 2012.

Richter, T.: Sedimentary fluxes at the Mid-Atlantic Ridge: sediment sources, accumulation rates, and geochemical characterisation, Ph.D. thesis, Christian-Albrechts-Universität, Kiel, https://doi.org/10.3289/GEOMAR_REP_73_1998, 1998.

Richter, T.: Age model and sedimentation rates of core GEOFAR KF13, https://doi.org/10.1594/PANGAEA.66315, 2001.

Romero, O. E., Mollenhauer, G., Schneider, R. R., and Wefer, G.: Radiocarbon (14C) AMS dating of sediment core GeoB3606-1, https://doi.org/10.1594/PANGAEA.80893, 2003.

Rühlemann, C., Mulitza, S., Müller, P. J., Wefer, G., and Zahn, R.: Warming of the tropical Atlantic Ocean and slowdown of thermohaline circulation during the last deglaciation, Nature, 402, 511–514, https://doi.org/10.1038/990069, 1999.

Santos, T. P. d., Lessa, D. V. d. O., Venancio, I. M., Chiessi, C. M., Mulitza, S., Kuhnert, H., Govin, A., Machado, T., Costa, K. B., Toledo, F. A. L., Dias, B. B., and Albuquerque, A. L. S.: (Supplementary Table 1) 14C datings of sediment core GL1090, https://doi.org/10.1594/PANGAEA.871875, 2017.

https://doi.org/10.5194/egusphere-2026-2299
Preprint. Discussion started: 24 June 2026

Saraswat, R., Lea, D. W., Nigam, R., Mackensen, A., and Naik, D. K.: Deglaciation in the tropical Indian Ocean driven by interplay between the regional monsoon and global teleconnections, Earth and Planetary Science Letters, 375, 166–175, https://doi.org/10.1016/j.epsl.2013.05.022, 2013.

Sarnthein, M., Winn, K., Jung, S. J. A., Duplessy, J.-C., Labeyrie, L., Erlenkeuser, H., and Ganssen, G.: Changes in East Atlantic Deepwater Circulation over the last 30,000 years: Eight time slice reconstructions, Paleoceanography, 9, 209–267, https://doi.org/https://doi.org/10.1029/93PA03301, 1994.

Schmidt, M. W., Chang, P., Hertzberg, J. E., Them, T. R., Ji, L., and Otto-Bliesner, B. L.: Impact of abrupt deglacial climate change on tropical Atlantic subsurface temperatures, Proceedings of the National Academy of Sciences, 109, 14 348–14 352, https://doi.org/10.1073/pnas.1207806109, 2012.

Schröder, J. F., Kuhnt, W., Holbourn, A., Beil, S., Zhang, P., Hendrizan, M., and Xu, J.: Deglacial Warming and Hydroclimate Variability in the Central Indonesian Archipelago, Paleoceanography and Paleoclimatology, 33, 974–993, https://doi.org/10.1029/2018PA003323, 2018.

Schwab, C., Kinkel, H., Weinelt, M., and Repschläger, J.: (Table S1) Age determination of sediment cores of the Azores Current System, https://doi.org/10.1594/PANGAEA.824858, 2012.

Seidenkrantz, M.-S., Kuijpers, A., Olsen, J., Pearce, C., Lindblom, S., Ploug, J., Przybyło, P., and Snowball, I.: Southwest Greenland shelf glaciation during MIS 4 more extensive than during the Last Glacial Maximum, Scientific Reports, 9, 15 617, https://doi.org/https://doi.org/10.1038/s41598-019-51983-3, 2019.

Shackleton, N., Imbrie, J., and Hall, M.: Oxygen and carbon isotope record of East Pacific core V19-30: implications for the formation of deep water in the late Pleistocene North Atlantic, Earth and Planetary Science Letters, 65, 233–244, https://doi.org/10.1016/0012-821X(83)90162-0, 1983.

Shackleton, N., Fairbanks, R., chien Chiu, T., and Parrenin, F.: Absolute calibration of the Greenland time scale: implications for Antarctic time scales and for d14C, Quaternary Science Reviews, 23, 1513–1522, https://doi.org/https://doi.org/10.1016/j.quascirev.2004.03.006, 2004.

Shackleton, N. J., Hall, M. A., and Vincent, E.: Phase relationships between millennial-scale events 64,000–24,000 years ago, Paleoceanography, 15, 565–569, https://doi.org/https://doi.org/10.1029/2000PA000513, 2000.

Singer, B. S.: A Quaternary geomagnetic instability time scale, Quaternary Geochronology, 21, 29–52, https://doi.org/https://doi.org/10.1016/j.quageo.2013.10.003, quaternary Geochronology Special Issue: Advances in 40Ar/39Ar Dating of Quaternary Events and Processes, 2014.

Singh, A. D., Jung, S. J. A., Darling, K. F., Ganeshram, R. S., Ivanochko, T. S., and Kroon, D.: (Table S1) Age determination of sediment cores SK99_17 and MD76-131, https://doi.org/10.1594/PANGAEA.829978, 2011.

Sirocko, F., Sarnthein, M., Erlenkeuser, H., Lange, H., Arnold, M., and Duplessy, J.-C.: Age determination of sediment core SO42-74KL from the Arabian Sea (Table 1), https://doi.org/10.1594/PANGAEA.407912, 1993.

Skinner, L. and Shackleton, N.: An Atlantic lead over Pacific deep-water change across Termination I: implications for the application of the marine isotope stage stratigraphy, Quaternary Science Reviews, 24, 571–580, https://doi.org/10.1016/j.quascirev.2004.11.008, 2005.

Skinner, L. C. and Shackleton, N. J.: Rapid transient changes in northeast Atlantic deep water ventilation age across Termination I, Paleoceanography, 19, 2003PA000 983, https://doi.org/10.1029/2003PA000983, 2004.

Skinner, L. C., Shackleton, N. J., and Elderfield, H.: Millennial-scale variability of deep-water temperature and δ^{18} O_{dw} indicating deep-water source variations in the Northeast Atlantic, 0–34 cal. ka BP, Geochemistry, Geophysics, Geosystems, 4, 2003GC000 585, https://doi.org/10.1029/2003GC000585, 2003.

https://doi.org/10.5194/egusphere-2026-2299
Preprint. Discussion started: 24 June 2026

Sortor, R. N. and Lund, D. C.: No evidence for a deglacial intermediate water Δ14C anomaly in the SW Atlantic, Earth and Planetary Science Letters, 310, 65–72, https://doi.org/10.1016/j.epsl.2011.07.017, 2011.

Spooner, M. I., De Deckker, P., Barrows, T. T., and Fifield, L. K.: The behaviour of the Leeuwin Current offshore NW Australia during the last five glacial–interglacial cycles, Global and Planetary Change, 75, 119–132, https://doi.org/10.1016/j.gloplacha.2010.10.015, 2011.

Spratt, R. M. and Lisiecki, L. E.: A Late Pleistocene sea level stack, Climate of the Past, 12, 1079–1092, https://doi.org/10.5194/cp-12-1079-2016, 2016.

Stern, J. V. and Lisiecki, L. E.: North Atlantic circulation and reservoir age changes over the past 41,000,years, Geophysical Research Letters, 40, 3693–3697, https://doi.org/10.1002/grl.50679, 2013.

Stott, L., Timmermann, A., and Thunell, R.: Southern Hemisphere and Deep-Sea Warming Led Deglacial Atmospheric CO_2 Rise and Tropical Warming, Science, 318, 435–438, https://doi.org/10.1126/science.1143791, 2007.

Sun, Y., Oppo, D. W., Xiang, R., Liu, W., and Gao, S.: Last deglaciation in the Okinawa Trough: Subtropical northwest Pacific link to Northern Hemisphere and tropical climate, Paleoceanography, 20, 2004PA001 061, https://doi.org/10.1029/2004PA001061, 2005.

Süli, E. and Mayers, D. F.: An Introduction to Numerical Analysis, Cambridge University Press, 2003.

Thornalley, D. J. R., Barker, S., Broecker, W. S., Elderfield, H., and McCave, I. N.: The Deglacial Evolution of North Atlantic Deep Convection, Science, 331, 202–205, https://doi.org/10.1126/science.1196812, 2011.

Tian, J., Huang, E., and Pak, D. K.: East Asian winter monsoon variability over the last glacial cycle: Insights from a latitudinal sea-surface temperature gradient across the South China Sea, Palaeogeography, Palaeoclimatology, Palaeoecology, 292, 319–324, https://doi.org/10.1016/j.palaeo.2010.04.005, 2010.

Venancio, I. M., Mulitza, S., Govin, A., Santos, T. P. d., Lessa, D. V. d. O., Albuquerque, A. L. S., Chiessi, C. M., Tiedemann, R., Vahlenkamp, M., Bickert, T., and Schulz, M.: Radiocarbon age determination of sediment core GL-1248, https://doi.org/10.1594/PANGAEA.895048, 2018.

Vidal, L., Schneider, R. R., Marchal, O., Bickert, T., Stocker, T. F., and Wefer, G.: (Table 2) Age determination of sediment core GeoB1711-4, https://doi.org/10.1594/PANGAEA.56993, 1999.

Voigt, I., Chiessi, C. M., Prange, M., Mulitza, S., Groeneveld, J., Varma, V., and Henrich, R.: (Table 2) Accelerator mass spectrometry radiocarbon dates and calibrated ages used in the age-depth models of sediment cores GeoB6211, GeoB13862-1 and GeoB6308, https://doi.org/10.1594/PANGAEA.841894, 2015.

Waelbroeck, C., Lougheed, B. C., Vazquez Riveiros, N., Missiaen, L., Pedro, J., Dokken, T., Hajdas, I., Wacker, L., Abbott, P., Dumoulin, J.-P., Thil, F., Eynaud, F., Rossignol, L., Fersi, W., Albuquerque, A. L., Arz, H., Austin, W. E. N., Came, R., Carlson, A. E., Collins, J. A., Dennielou, B., Desprat, S., Dickson, A., Elliot, M., Farmer, C., Giraudeau, J., Gottschalk, J., Henderiks, J., Hughen, K., Jung, S., Knutz, P., Lebreiro, S., Lund, D. C., Lynch-Stieglitz, J., Malaizé, B., Marchitto, T., Martínez-Méndez, G., Mollenhauer, G., Naughton, F., Nave, S., Nürnberg, D., Oppo, D., Peck, V., Peeters, F. J. C., Penaud, A., Portilho-Ramos, R. D. C., Repschläger, J., Roberts, J., Rühlemann, C., Salgueiro, E., Sanchez Goni, M. F., Schönfeld, J., Scussolini, P., Skinner, L. C., Skonieczny, C., Thornalley, D., Toucanne, S., Rooij, D. V., Vidal, L., Voelker, A. H. L., Wary, M., Weldeab, S., and Ziegler, M.: Consistently dated Atlantic sediment cores over the last 40 thousand years, Scientific Data, 6, 165, https://doi.org/10.1038/s41597-019-0173-8, 2019.

Wan, S. and Jian, Z.: Deep water exchanges between the South China Sea and the Pacific since the last glacial period, Paleoceanography, 29, 1162–1178, https://doi.org/10.1002/2013PA002578, 2014.

Wang, L., Sarnthein, M., Erlenkeuser, H., Grimalt, J. O., Grootes, P. M., Heilig, S., Ivanova, E. V., Kienast, M., Pelejero, C., and Pflaumann, U.: Age determination of sediments core GIK17961-2, https://doi.org/10.1594/PANGAEA.726161, 1999a.

https://doi.org/10.5194/egusphere-2026-2299
Preprint. Discussion started: 24 June 2026

Wang, L., Sarnthein, M., Erlenkeuser, H., Grimalt, J. O., Grootes, P. M., Heilig, S., Ivanova, E. V., Kienast, M., Pelejero, C., and Pflaumann, U.: Age determination of sediments core GIK17964-2, https://doi.org/10.1594/PANGAEA.726162, 1999b.

Wang, L., Sarnthein, M., Grootes, P. M., and Erlenkeuser, H.: Age determination of sediment core GIK17940-2, https://doi.org/10.1594/PANGAEA.736636, 1999c.

Wang, Y. V., Larsen, T., Leduc, G., Andersen, N., Blanz, T., and Schneider, R. R.: (Table 2) Age determination of sediment core GIK16160-3, https://doi.org/10.1594/PANGAEA.803746, 2013.

Weldeab, S., Schneider, R. R., Kölling, M., and Wefer, G.: Holocene African droughts relate to eastern equatorial Atlantic cooling, Geology, 33, 981, https://doi.org/10.1130/G21874.1, 2005.

Weldeab, S., Lea, D. W., Schneider, R. R., and Andersen, N.: 155,000 Years of West African Monsoon and Ocean Thermal Evolution, Science, 316, 1303–1307, https://doi.org/10.1126/science.1140461, 2007.

Weldeab, S., Friedrich, T., Timmermann, A., and Schneider, R. R.: Strong middepth warming and weak radiocarbon imprints in the equatorial Atlantic during Heinrich 1 and Younger Dryas, Paleoceanography, 31, 1070–1082, https://doi.org/10.1002/2016PA002957, 2016.

Westerhold, T., Agnini, C., Anagnostou, E., Hilgen, F., Hönisch, B., Meckler, A. N., Pälike, H., Wade, B., Sosdian, S., and Kasbohm, J.: Timing Is Everything, Paleoceanography and Paleoclimatology, 39, e2024PA004 932, https://doi.org/https://doi.org/10.1029/2024PA004932, e2024PA004932 2024PA004932, 2024.

Williams, C., Flower, B. P., Hastings, D. W., Guilderson, T. P., Quinn, K. A., and Goddard, E. A.: Deglacial abrupt climate change in the Atlantic Warm Pool: A Gulf of Mexico perspective: DEGLACIAL CLIMATE IN THE ATLANTIC WARM POOL, Paleoceanography, 25, n/a–n/a, https://doi.org/10.1029/2010PA001928, 2010.

Wolpert, R. L.: Lecture Notes on Stationary Gamma Processes, https://arxiv.org/abs/2106.00087, 2021.

Zhang, Y., Chiessi, C. M., Mulitza, S., Zabel, M., Trindade, R. F., Hollanda, M. H. B. M., Dantas, E. L., Govin, A., Tiedemann, R., and Wefer, G.: (Table 2) Raw 14C AMS data and calibrated ages of sediment cores GeoB16206-1 and GeoB16224-1, https://doi.org/10.1594/PANGAEA.853988, 2015.

Zhou, Y., McManus, J. F., Jacobel, A. W., Costa, K. M., Wang, S., and Alvarez Caraveo, B.: Enhanced iceberg discharge in the western North Atlantic during all Heinrich events of the last glaciation, Earth and Planetary Science Letters, 564, 116 910, https://doi.org/https://doi.org/10.1016/j.epsl.2021.116910, 2021.